This is a preprint, the final version is subject to change, of the American Mineralogist (MSA)
Cite as Authors (Year) Title. American Mineralogist, in press.
(DOI will not work until issue is live.) DOI: http://dx.doi.org/10.2138/am-2017-5915

Revision 1

Using mineral equilibria to estimate H_2O activities in peridotites from the Western Gneiss Region of Norway

Patricia Kang

Dept. of Geology & Geophysics
Texas A&M University,
College Station, TX 77843, U.S.A.

William M Lamb

Dept. of Geology & Geophysics
Texas A&M University,
College Station, TX 77843, U.S.A.

Martyn Drury

Dept. of Earth Sciences
Utrecht University,
Utrecht, CD 3584, Netherlands

Running Title: H_2O content of orogenic mantle peridotites

Corresponding Author, email: ww-lamb@geos.tamu.edu; Phone: 979-845-3075; Fax: 979-845-6162

This is a preprint, the final version is subject to change, of the American Mineralogist (MSA)
Cite as Authors (Year) Title. American Mineralogist, in press.
(DOI will not work until issue is live.) DOI: http://dx.doi.org/10.2138/am-2017-5915

Abstract

The earth's mantle is an important reservoir of H_2O, and even a small amount of H_2O has a significant influence on the physical properties of mantle rocks. Estimating the amount of H_2O in rocks from the earth's mantle would, therefore, provide some insights into the physical properties of this volumetrically dominant portion of the earth. The goal of this study is to use mineral equilibria to determine the activities of H_2O (aH_2O) in orogenic mantle peridotites from the Western Gneiss Region of Norway. An amphibole dehydration reaction yielded values of aH_2O ranging from 0.1 to 0.4 for these samples. Values of fO_2 of approximately 1 to 2 log units below the FMQ oxygen buffer were estimated from a fO_2-buffering reaction between olivine, orthopyroxene, and spinel for these same samples. These results demonstrate that the presence of amphibole in the mantle does not require elevated values of aH_2O (i.e., $aH_2O \approx 1$) nor relatively oxidizing values of fO_2. (i.e., > FMQ).

It is possible to estimate a minimum value of aH_2O by characterizing fluid speciation in C-O-H system for a given value of oxygen fugacity (fO_2). Our results show that the estimates of aH_2O obtained from the amphibole dehydration equilibrium are significantly lower than values of aH_2O estimated from this combination of fO_2 and C-O-H calculations. This suggests that fluid pressure (P_{fluid}) is less than lithostatic pressure (P_{lith}) and, for metamorphic rocks, implies the absence of a free fluid phase.

Fluid absent condition could be generated by amphibole growth during exhumation. If small amounts of H_2O were added to these rocks, the formation of amphibole could yield low values of aH_2O by consuming all available H_2O. On the other hand, if the nominally anhydrous minerals (NAMs) contained significant H_2O at conditions outside of the stability field of amphibole they might have served as a reservoir of H_2O. In this case, NAMs could supply the

63 OH necessary for amphibole growth once retrograde P-T conditions were consistent with
64 amphibole stability. Thus, amphibole growth may effectively dehydrate co-existing NAMs, and
65 enhance the strength of rocks as long as the NAMs controlled the rheology of the rock.
66
67 Key words: (6) amphibole equilibria; C-O-H fluid equilibria; H solubility; nominally anhydrous
68 minerals; mantle fluid; peridotite
69

Introduction

Peridotites are the dominant rock type in the earth's upper mantle and are a common constituent of orogenic zones. H_2O has a significant influence on the physical properties of peridotites. For example, small amounts of HH_2O also enhances ionic diffusion rate, thereby reducing the effective viscosity of minerals such as olivine (Hirth and Kohlstedt, 1996; Karato and Jung, 1998; Mei and Kohlstedt, 2000a, b). Given that modeling convection in the mantle requires constraints on viscosity of mantle peridotites (Solomatov, 1995; Moresi and Solomatov, 1998; Tackley, 1998), estimates of mantle H_2O content are required to model convection and determine the threshold amount of H_2O for the operation of plate tectonic style of convection (Moresi and Solomatov, 1998). Furthermore, the development of deformation microstructures in olivine may be related to it's OH content (Jung and Karato, 2001; Jung et al., 2006; Ohuchi et al., 2012), and, therefore, the interpretation of mantle seismic anisotropy may depend, to some extent, on the OH content of olivine (Nakajima and Hasegawa, 2004; Long and van der Hilst, 2005; Mainprice et al., 2005; Ohuchi et al., 2012).Clearly, determining the OH contents of the minerals in mantle peridotites will provide insight into various mantle properties and processes. Direct determination of the H_2O content of the mantle relies on the analysis of mantle peridotites, and these samples may be xenoliths or orogenic peridotites (i.e., masses of peridotite, presumably of mantle origin, that have been emplaced in the crust). The H_2O content of the minerals in mantle peridotites has been characterized by determining the amount of H contained in nominally anhydrous minerals (NAMs), such as olivine, pyroxene, and garnet. This characterization of mantle NAM OH content has largely been confined to xenoliths (Ingrin and Skogby, 2000; Bell et al., 2003; Maldener et al., 2003; Peslier and Luhr, 2005; Mosenfelder et al., 2006b; Peslier, 2010; Peslier et al., 2010; Sundvall and Skogby, 2011). A potential confounding effect, however,

is the possible diffusive loss of hydrogen during the emplacement of mantle rocks at the surface of the earth. This may be a particular problem for minerals from orogenic peridotites, which undergo slow cooling as compared to olivine contained in mantle xenoliths which undergo relatively rapid uplift and cooling (e.g., Ingrin and Skogby, 2000; Demouchy and Mackwell, 2006). Diffusion rates of H_2O in pyroxenes are probably significantly less than those in olivine (Bai and Kohlstedt, 1992; Bai and Kohlstedt, 1993) and Warren and Hauri (2014) argue that pyroxenes from orogenic peridotites may retain their pre-emplacement OH content while olivine from the same rocks may suffer significant H-loss. However, more research to fully characterize the diffusion rate of H in pyroxenes may be required before pyroxene OH contents may be used to confidently determine the OH contents of orogenic peridotites. Furthermore, the relation between values of aH_2O in peridotites and pyroxene OH contents (Skogby, 1994; Rauch and Keppler, 2002; Stalder et al., 2005; Stalder and Ludwig, 2007; Sundvall and Skogby, 2011) are not well known as compared to olivine (Gaetani et al., 2014).

H_2O may also be stored in hydrous phases, and amphibole may be the most common hydrous phase in the uppermost mantle. Mantle amphiboles have long been the object of petrologic investigations, particularly after Oxburgh (1964) suggested that the presence of this mineral in the upper mantle would explain the high K-content of mantle-derived basalts, and mantle amphiboles often form via the interaction of mantle rocks with mantle fluids. A wide variety of fluid types may be involved in the process of mantle metasomatism, including silicate and carbonatite melts, as well as dense brines and C-O-H fluids (Agrinier et al., 1993; Ionov and Hofmann, 1995; Vannucci et al., 1995; Niida and Green, 1999; Ionov et al., 2002; Coltorti et al., 2004; Powell et al., 2004), and more than one of these fluid types have been implicated in the formation of mantle amphiboles (see O'Reilly and Griffin, 2013, and references therein).

Investigation of the crystal chemistry of mantle amphiboles has revealed that many contain significant amounts of Fe^{3+}, which is inversely correlated with the H-content (Popp and Bryndzia, 1992; Dyar et al., 1993). This has led to the experimental investigation of amphibole dehydrogenation (oxidation) equilibria, which have been to estimate the fugacity of hydrogen in mantle rocks. This method is based on a reaction that involves the oxidation of Fe^{2+} to Fe^{3+} with the concomitant loss of H from the amphibole. Popp et al. (1995; 2006) experimentally calibrated a single dehydrogenation reaction using three different amphibole compositions over a range of T, P, and fH_2. As a result, if the T, P and chemical composition of the amphibole are known the fH_2 in the environment of equilibration can be estimated from the iron oxy/hydroxy proportions in the amphibole. Mineral equilibria have also been used to estimate values of fO_2 for a variety of mantle rocks, including mantle xenoliths (Wood and Virgo, 1989; Woodland and Koch, 2003; McCammon and Kopylova, 2004) and orogenic peridotites (Woodland et al., 1992), and these values have been used to constrain the compositions of mantle fluids (Bryndzia and Wood, 1990; Wood et al., 1990). Thus, for peridotites containing mantle amphiboles that co-exist with orthopyroxene, olivine and spinel and/or garnet it is possible to estimate values of both fO_2 and fH_2 and use these values to estimate values of fH_2O (Popp et al., 2006).

H_2O-buffering amphibole (pargasite) dehydration equilibria have also been used to estimate the activity of H_2O (aH_2O) in the mantle (Popp et al., 2006; Lamb and Popp, 2009; Bonadiman et al., 2014; Gentili et al., 2015). Lamb and Popp (2009) demonstrated that values of aH_2O estimated from amphibole dehydration equilibria are not as sensitive to partial H-loss from amphibole via diffusion as compared to values of aH_2O estimated from the combination of fH_2 and fO_2 described above (Lamb and Popp, 2009). Thus, dehydration equilibria may be a particularly appropriate method to apply to estimate values of aH_2O from orogenic peridotites.

This paper applies amphibole (pargasite) dehydration equilibrium to estimate values of aH_2O in orogenic mantle peridotites from the Western Gneiss region of Norway. These estimates require an independent determination of the P-T of amphibole equilibration and, therefore, this study helps constrain the relative timing of amphibole growth. Values of oxygen fugacity (fO_2), estimated for these same rocks, were used to constrain the activities of a variety of fluid species in the C-O-H system, including H_2O, CO_2, CH_4, H_2, and CO (Lamb and Valley, 1984; Lamb and Valley, 1985; Zhang and Duan, 2009). These values of fO_2, in combination with the estimated values of aH_2O, permit us to determine if a lithostatically pressured C-O-H fluid phase was present at the time of mineral equilibration.

Geologic And Petrologic Background

The Western Gneiss Region (WGR) of Norway is part of the Norwegian Caledonides which covers an area of approximately 5×10^4 km^2 between Bergen and Trondheim (Fig. 1). The WGR lies within a tectonic window and is surrounded by thick piles of allochthonous tectonic nappes that migrated eastwards onto Baltica during the continental collision between Baltica and Laurentia (Roberts and Gee, 1985). The subduction of Baltica, which occurred during the Scandian orogeny, produced minerals that are stable under ultra-high pressure (UHP) metamorphic conditions (Smith, 1984; Brueckner et al., 2002; Van Roermund et al., 2002; Vrijmoed et al., 2006).

A number of orogenic garnet peridotites are exposed within the WGR (Carswell, 1986; Drury et al., 2001; Spengler et al., 2006; van Roermund, 2009). In rare cases certain peridotite bodies from this region retain evidence of having been exposed to extreme P-T conditions during the Archean and may also preserve evidence of recrystallization and re-equilibration during the Proterozoic (Carswell and Van Roermund, 2005; Spengler et al., 2006; Spengler et al., 2009; van

Roermund, 2009). During the Scandian Orogeny, these peridotites (Fig. 1) became incorporated into the subducting Baltican continental crust (Spengler et al., 2006; van Roermund, 2009). Ongoing subduction of the Baltican crust caused the minerals in the peridotites to undergo the peak metamorphic P-T condition of 5.5-6.5 Gpa and 870-920°C (Spengler et al., 2009). During subsequent uplift and cooling, a neoblastic assemblage that is characterized by a smaller grain size and a strong preferred orientation, was stabilized. P-T estimates using the core compositions of small orthopyroxenes (< 0.3 mm) and other minerals in this assemblage are 3.8-4 GPa and 820-880°C (Spengler et al., 2009). Continued exhumation produced additional minerals, including matrix amphiboles and an intergrowth of spinel, pyroxenes, and amphibole that surrounds garnet, a texture commonly referred to as kelyphite (Carswell, 1986; Spengler et al., 2009; van Roermund, 2009). This Scandian overprint is extensively recognized within the northernmost part of the Western Gneiss Region (van Roermund, 2009). The amphibole-bearing mineral assemblages investigated in this study formed during cooling and depressurization following the UHP event.

Analytical Procedure

The compositions of the minerals in the samples were analyzed using a Cameca SX-50 electron microprobe located in the Department of Geology at Texas A&M University. Analyses were conducted using an accelerating voltage of 15 kV and beam current of 20 nA. The beam diameter was 1 μm for the analyses of olivine, orthopyroxene, clinopyroxene, garnet, and spinel, and 10 μm for the analysis of amphibole.

Olivine and spinel, pyroxene, and garnet analyses were normalized to three, four, and eight cations, respectively. However, amphibole normalization required the quantification of three unknowns: 1) the ratio of Fe^{3+} to Fe^{2+}, 2) oxy/hydroxy content, and 3) vacancies on the

crystallographic A-site. Since conventional probe analyses do not provide these values, we used the normalization procedure described in Lamb and Popp (2009). This procedure requires a value of $Fe^{3+}/\Sigma Fe$, where $\Sigma Fe = Fe^{3+} + Fe^{2+}$, and the use of empirically derived relations between the cation content and the oxy/hydroxyl content of mantle amphibole to determine the amount of oxy/hydroxy components. However, in this study, values of $Fe^{3+}/\Sigma Fe$ were not estimated for amphiboles, and, therefore, amphibole normalization was performed by assuming the minimum ratio of $Fe^{3+}/\Sigma Fe$ that produced a charge-balanced formula. Given this compositional information, a conventional microprobe analysis and a value of $Fe^{3+}/\Sigma Fe$, an iterative approach is used to determine a chemical formula that satisfies the charge balance as well as the constraints on the crystallographic site occupancies (for details, see Lamb and Popp, 2009).

A redox equilibrium between olivine, orthopyroxene, and spinel was used to determine the values of oxygen fugacities (fO_2) (Wood, 1990), and these values depend strongly upon the value of $Fe^{3+}/\Sigma Fe$ in spinel. Determining the oxidation state of Fe in spinel via charge balance using conventional microprobe analyses may result in large uncertainties (Wood and Virgo, 1989; Woodland et al., 1992; Canil and O'Neill, 1996). These uncertainties are not entirely random, but, to some extent, they arise from systematic uncertainties in the chemical composition of the standard and/or uncertainties in matrix corrections (Wood and Virgo, 1989; Canil and O'Neill, 1996). However, it is possible to correct the values of $Fe^{3+}/\Sigma Fe$ in spinel originally determined via charge balance by using secondary spinel standards with known values of $Fe^{3+}/\Sigma Fe$ (Wood and Virgo, 1989). We applied this approach using secondary standards of spinels with $Fe^{3+}/\Sigma Fe$ values ranging from 0.15 to 0.31, as determined by Mössbauer Spectroscopy (standards provided by B. Wood).

Replicate analyses of these secondary spinel standards shows that, over the range of $Fe^{3+}/\Sigma Fe$ = 0.15 to 0.31, charge balance yields values of $Fe^{3+}/\Sigma Fe$ that are typically 0.05 to 0.08 larger than the values determined by Mössbauer Spectroscopy (for the standards employed in this study). Furthermore, this difference increases with increasing values of $Fe^{3+}/\Sigma Fe$. Charge balance yields $Fe^{3+}/\Sigma Fe$ values ranging from 0.03 to 0.07 for spinels from the samples in this study analyzed in this study. Correcting these values of $Fe^{3+}/\Sigma Fe$ using the analyses of secondary standards yielded values of $Fe^{3+}/\Sigma Fe$ that were even smaller, and in some cases, approximately equal to 0. However, this correction requires significant extrapolation from 0.15, the lowest value of $Fe^{3+}/\Sigma Fe$ of our spinel standards, to 0.03. Thus, in subsequent sections of this paper, we used $Fe^{3+}/\Sigma Fe$ values that were determined via charge balance. These are treated as maximum values because corrections based on the analyses of secondary standards, although uncertain, always yielded values of $Fe^{3+}/\Sigma Fe$ even smaller than the values estimated using charge balance.

Mineral modes in one of our samples (DS0286) were estimated using image analyses. An optical micrograph of the entire thin section was traced on a transparent paper along mineral boundaries, each of which was checked and identified with optical microscopy and related BSE images. The traced image was then scanned, and minerals were color-coded. Modal abundance of each mineral species was determined with an image-processing program (Image J; available at http://rsb.info.nih.gov/ij; developed by Wayne R, National Institutes of Health, Bethesda, MD). These modal percentages were converted into weight percentages (wt%) by using the values of mineral density at standard state, as estimated with the MELTS software package (Ghiorso and Sack, 1995; Asimow and Ghiorso, 1998).

Mineral Chemistry

Four different samples were collected from Otrøy Island in the Western Gneiss Region of Norway. All samples consisted of abundant olivines and orthopyroxenes with lesser amounts of coarse-grained garnets, clinopyroxenes, amphiboles, and spinels (Fig. 2a). The garnets were surrounded by a fibrous intergrowth of orthopyroxene, clinopyroxene, and spinel with minor amounts of amphibole (kelyphite) (Fig. 3). The retrograde reaction rims of kelyphite were enveloped again by a thin rim of orthopyroxenes and this rim of orthopyroxenes is referred to as 'COR' (Coarse Orthopyroxene Rim) (Obata and Ozawa, 2011). Small nodular spinels were sometimes located between these two reaction rims (Fig. 2b). Orthopyroxenes, clinopyroxenes, amphiboles, and spinels occur as matrix phases (Fig. 2a), and matrix clinopyroxenes were, in some cases, replaced by amphiboles (Fig. 2c).

Microprobe analyses reveal that various minerals in our samples exhibit compositional zoning, consistent with observations reported in previous studies (Medaris, 1984; Carswell, 1986; Spengler et al., 2009; van Roermund, 2009). Examples of this compositional variation are given in Figures 4 through 6, which plot cations per formula unit against distance across a single mineral grain.

The small size of minerals within the kelyphite made chemical characterization with the electron microprobe challenging and were restricted to the kelyphite grains at least 5 μm across in an effort to avoid excitation of x-rays from adjacent minerals. Mineral analyses and normalized outcomes for matrix minerals as well as minerals within the kelyphite are given in the electronic supplementary material.

Garnet

Garnet in each sample exhibits distinctive compositional zoning (Fig. 4). Garnet in NUM9a has complex compositional zoning with a relatively homogenous core and more abrupt

changes in chemical composition toward the rims (Fig. 4a and Fig. 4b). This garnet, in particular, preserves a relatively large decrease in Cr and coincident increase in Al starting approximately 25 μm from the rim. This trend is then reversed with an increase in Cr content and coincident decrease in Al within approximately 15 μm from the rim (Fig. 4b). These sharp changes in Al and Cr contents occur within a few tens of microns from the rims and are not preserved in other samples. For example, compositional changes are gradual across garnets in NRTP4 and DS0260, but Mg abruptly decreases and Fe sharply increases within the outermost ≈ 140 μm (NRTP4) and ≈ 300 μm (DS0260) of the rims (Fig. 4c and Fig. 4d). Garnet in NRTP4 displays a progressive decrease in Al and a gradual increase in Cr within ≈ 310 μm of the rim, while garnet in DS0260 shows opposite trends for these elements (Fig. 4c and Fig. 4d). In DS0286, garnet is relatively homogenous for analyzed oxides as compared to garnet in other samples (Table 1). For example, a garnet from sample DS0286 has the following average and 1σ standard deviation values for various oxides: 9.26 ± 0.16 wt% FeO, 19.09 ± 0.11 wt% MgO, and 4.96 ± 0.12 wt% CaO. Garnet in NRTP4 (Fig. 4c) is significantly less homogeneous with averages and 1σ standard deviations of 9.32 ± 0.38 wt% FeO, 18.54 ± 0.31 wt% MgO, and 5.47 ± 0.23 wt% CaO (electronic supplementary material 1).

Spinel

Matrix spinels typically exhibit a gradual decrease in Cr and an increase in Al from core to rim (Fig. 5a). Spinel inter-growths within the kelyphite rims are rich in Al compared to matrix spinels. For instance, in NRTP4 a single grain of spinel within the kelyphite contains 57.83 wt% Al_2O_3, as compared to the amount of Al_2O_3 in matrix spinels, which ranges from 18.02 to 29.78 wt% (electronic supplementary material 2).

Orthopyroxene

Matrix orthopyroxenes are characterized by relatively homogenous core compositions with decreasing Mg and increasing Al toward their rims (Fig. 5b). Orthopyroxene growing within the kelyphite has much higher Al_2O_3 contents (ranging from 1.96 to 13.74 wt%; electronic supplementary material 3) as compared to matrix orthopyroxenes (ranging from 0.28 to 1.86 wt%; electronic supplementary material 3).

The compositions of relatively small grains of orthopyroxenes that surround the kelyphite (COR) change gradually across the entire grains. The inner part of the COR, adjacent to the kelyphite is relatively similar in composition to the orthopyroxene within the outer part of the kelyphite (Table 2). However, the compositions of the outer part of the COR, adjacent to the matrix, are relatively similar to the rims of matrix orthopyroxene (Table 2).

Clinopyroxene

Matrix clinopyroxenes are compositionally zoned with increasing Ca and Mg and decreasing Na and Al toward the rims (Fig. 5c). These compositional variations are greater in clinopyroxene grains from NUM9a and NRTP4 as compared to those in our other samples (electronic supplementary material 4). Clinopyroxenes that are partially replaced by amphibole are compositionally homogenous.

Clinopyroxene within the kelyphite typically has higher Al_2O_3 contents (ranging from 1.78 to 8.65 wt%; electronic supplementary material 4) as compared to matrix clinopyroxene (ranging from 0.84 to 2.92 wt%; electronic supplementary material 4).

Amphibole

Matrix amphiboles in our samples (Table 3) are relatively homogenous including those that partially replace matrix clinopyroxene (Table 4). Matrix amphiboles in the proximity of the

298 kelyphite, however, show slight compositional zoning especially toward those rims in relatively
299 close proximity to the kelyphite (Table 3; Fig. 5d; distance ≈ 1240 μm). Amphibole forming
300 within the kelyphite has higher Al_2O_3 content (ranging from 14.64 to 15.94 wt%; electronic
301 supplementary material 5) than matrix amphibole.

302 **Interpretation of textures and compositional zoning**

303 Garnet-bearing peridotites in the Western Gneiss Region of Norway have a protracted
304 history that includes UHP metamorphism and subsequent uplift from a depth of approximately
305 200 km (Medaris, 1984; Carswell, 1986; Spengler et al., 2009; van Roermund, 2009). This
306 history is recorded by a sequence of mineral assemblages and/or compositional zoning within
307 individual minerals that had been produced through time and documented in a number of studies
308 (e.g., Medaris, 1984; Carswell, 1986; Spengler et al., 2009; van Roermund, 2009). These studies
309 established the P-T conditions of retrograde metamorphism for the samples examined in this
310 study. However, in order to apply mineral equilibria to estimate values of aH_2O and fO_2 it is
311 critical to determine the composition of each mineral, within compositionally zoned minerals,
312 that represents equilibrium with amphibole.

313 Fine-grained olivine, orthopyroxene, clinopyroxene, and spinel in the matrix are
314 texturally consistent with the neoblastic assemblage that was formed during subduction related to
315 the Scandian Orogeny (Fig. 2a). Matrix orthopyroxenes preserve an Al-low core with an increase
316 in Al near rims (Fig. 5b). These compositional trends are similar to those of orthopyroxene
317 grains that were interpreted to re-crystallize during Scandian subduction (Carswell, 1986;
318 Spengler et al., 2009). Spengler et al. (2009) described the increase in Al near rims of
319 orthopyroxene as reflecting re-equilibration during exhumation stages.

Partial replacement of matrix clinopyroxene by amphibole (Fig. 2c) suggests that matrix amphibole post-dates clinopyroxene. This partially replaced matrix clinopyroxene is similar in compositions to the rim of matrix clinopyroxene with no evidence of amphibole replacement. Thus, the rim compositions of the matrix clinopyroxene likely equilibrated with amphibole.

The textural similarity between matrix orthopyroxene and clinopyroxene (Fig. 2a) suggests they shared the same evolutionary history. This, combined with their close proximity indicates that rim compositions of two pyroxenes likely reflect equilibration during uplift. A similar argument can be made for matrix spinels, as they share proximity and textural similarity with matrix pyroxenes. Thus, given our previous argument that amphiboles are in equilibrium with clinopyroxene rims, estimates of P, T, aH_2O, and fO_2 that are based on mineral equilibria should be made using rim compositions of pyroxenes and spinels.

Garnets, as compared to the matrix pyroxenes and spinels are typically large and have complex internal chemical variability (zoning). Garnet in NUM9a, for example, exhibits a sudden drop in Cr coincident with an increase in Al within 25 μm of the rim (Fig. 4b). This trend is reversed with a drop in Al and increase in Cr as the distance to the rim decreases (Fig. 4b). Although Cr and Al are distributed between various phases in peridotites (e.g., Voigt and von der Handt, 2011), spinel and garnet are enriched in these elements compared to pyroxenes and olivines. Spinel forms at the expense of garnet and, as pressure decreases, and Cr will be preferentially partitioned into spinel relative to garnet (Green and Ringwood, 1970; Klemme, 2004; Grütter et al., 2006). This suggests that the formation of spinel will result in a decrease in the Cr content of the garnet. If so, the compositions of the garnet with the lowest Cr content would correspond to the rim compositions of matrix spinel and, thus, best represent the equilibrium with amphibole.

Kelyphite replaces garnet, and its formation may produce compositional changes near the rims of garnet. Mineral constituents within the kelyphite are significantly richer in Al than the same minerals in the matrix (see previous description). Therefore, the formation of kelyphite may account for the sharp decrease in Al and concomitant increase in Cr that occurs within 15 μm of the rim in the garnet of NUM9a (Fig. 4b). However, because kelyphite replaces the outermost portions of garnets, any compositional variation developed prior to kelyphite formation, that may have been originally preserved in the outer rims of a garnet, may be lost if this portion of the garnet is consumed by the kelyphite forming reaction.

This loss of the strongly zoned portion of the garnet due to the growth of kelyphite minerals may explain why garnets with well-developed kelyphite rims have little internal compositional variation (e.g., Fig. 4c and Fig. 4d), as opposed to garnets with small or non-existent kelyphite rims. The garnet in sample NUM9a, for example has a relatively thin kelyphite rim and the outermost portion of this garnet preserves a sharp changes in Cr and Al contents as described previously (Fig. 4a and Fig. 4b). In NRTP4, the kelyphite rim is larger than that in sample NUM9a, and the zoning profiles of the garnet in this sample (Fig. 4c) do not exhibit the same abrupt changes in composition near the rims of this mineral as compared to the garnet in NUM9a. Relatively large changes in composition, similar to those found within 30 μm of the rim of garnets in NUM9a, may have once existed near garnet rims in NRTP4, however, this portion of the garnet may have been consumed to produce kelyphite.

In some cases the thickness of the kelyphite rims may vary along the circumference of a single garnet. For instance, traverse 1 and 2 (Fig. 6a) show the locations of two series of analyses that are approximately perpendicular to the rim of a garnet in sample NUM9a. The electron microprobe analyses performed along traverse 1 include compositions from a portion of the

garnet rim with little or no adjacent kelyphite. This portion of the garnet exhibits relatively large changes in composition, as the outermost portion of this garnet preserves a decrease in Cr with a coincident increase in Al, which is followed by an increase in Cr and a simultaneous decrease in Al from core to rim (Fig. 6b). The chemical composition of the same garnet along traverse 2 (Fig. 6a), which is adjacent to well-developed kelyphite, exhibits relatively little change in composition toward the rim (Fig. 6c). This correlation between the development of kelyphite and the general lack of core-to-rim chemical variation is consistent with the idea that the original rim of the garnet was consumed by the kelyphite forming reaction and this resulted in the loss of the strongly zoned portions of this mineral.

Although matrix amphiboles in close proximity to the kelyphite is similar in composition to amphiboles within the kelyphite (Table 5), most matrix amphibole compositions do differ from the compositions of amphibole in the kelyphite. This indicates that these two amphiboles, within the kelyphite and within the matrix, did not completely equilibrate and textures indicate that some amphibole was present prior to kelyphite formation. If the abrupt decrease in the Al content of the garnet relates to kelyphite formation then this suggests that the matrix amphibole formed prior to the decrease in Al content of garnet that is preserved near the rims in certain garnets (Fig. 4a and Fig. 4b). Thus, the textures and chemistries of garnets, amphiboles and other minerals suggest that the low Cr regions near the rims of certain garnets were likely produced by the production of matrix spinel but predate the formation of the kelyphite. This feature is clearly visible in sample NUM9a. Garnet within NRTP4 does exhibit a gradual decrease in Cr followed by its increase, which are coincident with a progressive increase and then a decrease in Al toward the rims (Fig. 4c). Garnets from DS0260 and DS0286 were more homogeneous with no well-defined minimum Cr-content near the rims. However, the subtle decline in Cr-content may

still be a sign of spinel formation. Furthermore, change in the amounts of other cations, such as Mg, also indicates mineral growth likely related to the development of matrix phases. Thus, the compositions of the outermost rims of the garnet in these two samples (Fig. 4d) are considered to be in equilibrium with the rims of other matrix phases, including amphibole.

In summary, textural and compositional evidence indicates that the rims of the matrix phases, clinopyroxene, orthopyroxenes, and spinel are in equilibrium with one another and in equilibrium with amphibole. The low-Cr region of garnets at or near the rims of these grains likely represents the composition in equilibrium with the rims of matrix phases. Olivines in all samples do not display any significant compositional zoning, and thus, the average of the compositions was used to determine the activity of Mg_2SiO_4 in olivine that is in equilibrium with amphiboles.

Pressure And Temperature Estimates

One of the goals of this study is to use (de)hydration equilibria involving amphibole to estimate values of aH_2O. The stability of any equilibria involving H_2O is a function of P, T, and aH_2O, and, therefore, estimating aH_2O requires an independent estimate of the P and T. Because this P-T determination must be independent of aH_2O it should not be based on equilibria involving a hydrous phase, such as amphibole. Various geothermobarometers are available for estimating the pressure and temperature conditions of garnet-bearing peridotites (O'Neill and Wood, 1979; Brey and Köhler, 1990; Taylor, 1998; Nimis and Taylor, 2000; Wu and Zhao, 2007; Nimis and Grütter, 2010). Among the widely used thermometers, Taylor's formulation of the two-pyroxene thermometer effectively reproduces experimental temperatures over wide ranges of composition and pressure (Taylor, 1998; Nimis and Grütter, 2010). According to Nimis and Grütter (2010), this formulation also agrees with Brey and Kohler's Ca-in-orthopyroxene

412 thermometer as modified by Nimis and Grütter (2010) to within ± 90 ˚C and with the
413 orthopyroxene-garnet thermometer (Nimis and Grütter, 2010) to within ± 70 ˚C. Thus, we
414 selected rim compositions of co-existing pyroxenes and applied Taylor's two-pyroxene
415 thermometer to estimate the temperature of mineral equilibration for each sample. The estimated
416 condition was compared to the conditions obtained from two other thermometers, i.e., the
417 modified Ca-in-orthopyroxene thermometer and the orthopyroxene-garnet thermometer, as
418 suggested by Nimis and Grütter (2010).

419 We used an Al-in-orthopyroxene barometer that was formulated by Nickel and Green
420 (1985) to estimate pressures. The reliability of their barometer has been supported by its ability
421 to reproduce experimental pressures and by the consistency of estimated results with local
422 geotherms (Grütter, 2009; Nimis and Grütter, 2010).

423 Results of P and T are given in Table 6. Temperatures estimated from Taylor's two-
424 pyroxene thermometer range from 700 to 780 ˚C. The temperature estimate for each sample is
425 consistent, within the uncertainties mentioned above, with temperature estimates based on the
426 Nimis and Grütter and the modified Brey and Kohler thermometers. This indicates that these
427 thermometers yield reliable estimates for the temperature of mineral equilibration for each
428 sample. Pressures range from 17 to 27 kbar. These P and T estimate are similar to the conditions
429 inferred during exhumation of the orogenic peridotites in the Otrøy Island as well as adjacent
430 Flemsøy and Moldefjord as determined by Spengler et al. (2009) (Fig. 7).

431

432

433 ## Estimating H_2O Activities Using Amphibole Dehydration Equilibria

Given an independently determined value of P and T, a number of equilibria involving H_2O can be written that may be used to estimate values of aH_2O. The accuracy of this estimation will depend, in part, upon the quality of the models used to calculate the activity-composition relations in minerals. It is important, therefore, to determine which activity models may be most suitable given the mineralogy and mineral compositions in our samples. Lamb and Popp (2009) and Popp et al. (2006) have applied dehydration equilibria to estimate values of aH_2O in mantle rocks and have considered a number of different H_2O-buffering reactions as well as various models that describe the activity composition relations in those minerals included in these H_2O buffering reactions. We have adopted their approach, and the following paragraph is a short discussion that describes this approach including their choice of H_2O-buffering reaction and activity models, however, more detail is contained in these earlier publications (Popp et al., 2006; Lamb and Popp, 2009).

When choosing the most appropriate H_2O-buffering equilibria Lamb and Popp (2009) and Popp et al. (2006) favor reactions in which the end-members generally constituted large fractions of the natural phases in any given sample. Given the relatively Mg-rich nature of many mantle minerals, for example, Mg end-members were typically preferred (e.g., Mg_2SiO_4 rather than Fe_2SiO_4 in olivine). Activity models designed specifically for mantle pressures, temperatures, and compositions were also preferred and, therefore, the MELTS software package was employed to estimate the end-member activities of forsterite, enstatite, diopside, jadeite, and spinel (Table 7; Ghiorso and Sack, 1995; Asimow and Ghiorso, 1998). However, the amphibole model developed for MELTS is based on the relatively simple Ca-Mg-Fe^{2+} system (Ghiorso and Evans, 2002). A more suitable amphibole model should include additional components that occur in significant amounts (e.g., Al). For example, Dale et al.'s (2005) a-X model, developed

457 for use with the THERMOCALC software model, is based on the relatively extensive
458 compositional system of Na_2O-CaO-FeO-MgO-Al_2O_3-SiO_2-H_2O-O (NCFMASHO). Furthermore,
459 this amphibole model uses a dataset based on the solvus between naturally-occurring amphibole
460 pairs, which makes it sensitive to the thermodynamics of co-existing phases (Dale et al., 2005).
461 The amphiboles in the samples of this study are pargasite-rich and the Dale et al. model is well
462 suited to amphibole of this composition. Thus, we chose the following amphibole dehydration
463 equilibria:

$$\mathrm{En} + 2\mathrm{Parg} = 4\mathrm{Di} + 2\mathrm{Jd} + 2\mathrm{Fo} + 2\mathrm{Sp} + 2\mathrm{H_2O} \qquad (1)$$

464 where En is enstatite, Parg is pargasite, Di is diopside, Jd is jadeite, Fo is forsterite, and Sp is
465 spinel, to estimate values of aH2O, as did Lamb and Popp (2009). The estimated activities of
466 pargasite component in our amphiboles were corrected in order to consider the solid solution
467 between OH, O^{2-}, F, and Cl in the Z site (Table 7; Lamb and Popp, 2009).

468 Determining values of aH_2O from the equilibrium of (1) requires the determination of the
469 activities of all mineral end members in natural phases. The equilibrium constant for this
470 equilibrium is given by:

471 $$K_{eq} = \frac{(a^{\text{clinopyroxene}}_{\text{CaMgSi2O6}})^4 \cdot \left(a^{\text{clinopyroxene}}_{\text{NaAlSi2O6}}\right)^2 \cdot (a^{\text{olivine}}_{\text{Mg2SiO4}})^2 \cdot (a^{\text{spinel}}_{\text{MgAl2O4}})^2 \cdot (a_{H_2O})^2}{\left(a^{\text{orthopyroxene}}_{\text{Mg2Si2O6}}\right) \cdot (a^{\text{amphibole}}_{\text{NaCa2Mg4Al3Si6O22(OH)2}})^2} \qquad (2)$$

472 Thus, the following end members were considered: Mg_2SiO_4 (forsterite) in olivine, $Mg_2Si_2O_6$
473 (enstatite) in orthopyroxene, $CaMgSi_2O_6$ (diopside) in clinopyroxene, $NaAlSi_2O_6$ (jadeite) in
474 clinopyroxene, $MgAl_2O_4$ (spinel) in spinel, and $NaCa_2Mg_4Al_3Si_6O_{22}(OH)_2$ (pargasite) in
475 amphibole. Lamb and Popp (2009) showed that there was often good agreement between the
476 activities of various end-members, such as forsterite in olivine and diopside in clinopyroxene, as
477 estimated from the a-X model of MELTS and the various models developed for
478 THERMOCALC, even though the two programs are based on different datasets. These

similarities suggest that THERMOCALC can be used in conjunction with activity models based on MELTS to estimate aH_2O for mantle conditions (Lamb and Popp, 2009). Therefore, THERMOCALC software was used to locate the dehydration reaction of (1) as a function of temperature, pressure, and aH_2O (Fig. 8). Values of aH_2O for all samples range from 0.12 to 0.34 (Table 7).

As discussed previously, the chemical composition of pargasite was normalized to yield the maximum OH content in Z-site by assuming a minimum value of $Fe^{3+}/\Sigma Fe$. This maximizes the value of $a^{\text{amphibole}}_{NaCa_2Mg_4Al_3Si_6O_{22}(OH)_2}$ and, therefore, the calculations based on equilibrium (1) yield maximum values of aH_2O. It might be argued that a more complete characterization of the amphibole chemistry is required when values of aH_2O are estimated using equilibria that involve this mineral. However, estimates of aH_2O using the approach described here are not strongly sensitive to the oxidation state of Fe in the amphibole (Lamb and Popp, 2009). For example, application of equilibrium (1) to sample NRTP4 yields a value of aH2O = 0.34 assuming Fe3+/ΣFe = 0 (Table 7). If the value of Fe3+/ΣFe is instead assigned a value of 0.5 then the value of aH_2O is 0.31, a decrease of 0.05. In the extreme case, if the Fe in the amphibole from sample NRTP4 was completely oxidized (Fe3+/ΣFe = 1.0) then application of equilibrium (1) would yield the $aH_2O = 0.26$. Thus, while our application of equilibrium (1) yields maximum values of aH_2O, these values are relatively low (< 0.4 in all cases). Furthermore, the amount by which our values of aH_2O may be overestimated is limited and is likely significantly less than 0.1.

Oxygen Fugacity Estimates

503 The oxygen fugacity (fO_2) of each sample was estimated relative to that of fayalite-
504 magnetite-quartz (FMQ) redox buffer using the following redox equilibria:

$$6Fe_2SiO_4(\text{olivine}) + O_2 = 3Fe_2Si_2O_6(\text{orthopyroxene}) + 2Fe_3O_4(\text{spinel}) \quad (3)$$

505 We chose to use the Wood version of this oxybarometer (Wood, 1990), which is given by:

$$\Delta\log(fO_2)^{FMQ} = 0.35 + \frac{220}{T(K)} - \frac{0.0369P(bars)}{T(K)} - 12\log\left(X_{Fe}^{olv}\right) - \frac{2620(X_{Mg}^{olv})^2}{T(K)}$$
$$+ 3\log\left(X_{Fe}^{M1}X_{Fe}^{M2}\right)^{opx} + 2\log\left(a_{Fe_3O_4}^{sp}\right) \quad (4)$$

506 where X_{Fe}^{olv}, X_{Mg}^{olv} are the mole fractions of Mg and Fe end-members in olivine, X_{Fe}^{M1}, X_{Fe}^{M2} are the
507 atomic fraction of Fe in the two different orthopyroxene sites (M1 and M2), and $a_{Fe_3O_4}^{sp}$ is the
508 activity of Fe_3O_4 in spinel. The results yield upper limits for values of fO_2 as charge-balanced
509 normalization yields the maximum value of $Fe^{3+}/\Sigma Fe$ for spinel composition as described in the
510 previous section (see the ANALYTICAL PROCEDURE section above). Estimated values of fO_2
511 range from 3.2 to 1.8 log units more reducing than the FMQ oxygen buffer (Table 7).

512 ## Fluid Equilibria In The C-O-H System

513 A number of researchers have used fluid equilibria to constrain activities (or fugacities)
514 of six different fluid species, H_2O, CO_2, CH_4, H_2, CO, and O_2, in the C-O-H system (French,
515 1966; Ohmoto and Kerrick, 1977; Lamb and Valley, 1984; Lamb and Valley, 1985; Connolly
516 and Cesare, 1993). These six fluid species can be related by four different reactions (e.g.,
517 Ohmoto and Kerrick, 1977):

$$C + O_2 = CO_2 \quad (5)$$
$$C + \frac{1}{2}O_2 = CO \quad (6)$$
$$H_2 + \frac{1}{2}O_2 = H_2O \quad (7)$$
$$CH_4 + 2O_2 = CO_2 + 2H_2O \quad (8)$$

518

519 Calculation of fluid speciation in this system has typically been performed in carbon (i.e.
520 graphite or diamond) bearing system such that aC is unity. In this case if the fugacity of one of
521 the fluid species is fixed, for example fO_2, then the fugacities of the remaining five fluid species
522 can be determined if an additional equation is written (i.e., five equations and five unknowns).
523 In many cases it is assumed that a free fluid phase, existing along mineral grain boundaries and
524 or triple junctions, is present and the fluid pressure (P_{fluid}) is equivalent to the lithostatic pressure
525 (P_{lith}) such that:

$$P_{lith} = P_{fluid} = P_{H_2O} + P_{CO_2} + P_{CH_4} + P_{CO} + P_{H_2} + P_{O_2} \qquad (9).$$

526 In this case, the pressure is typically inferred from mineral equilibria (i.e., geobarometry).

527 Calculations in the C-O-H system in which aC =1, $P_{fluid} = P_{lith}$, and fO_2 is fixed have
528 been performed by several researchers (e.g., French, 1966; Lamb and Valley, 1984; Lamb and
529 Valley, 1985). However, fixing the value of the fugacity of any on of the six fluid species, not
530 only oxygen, will permit simultaneous solution of equations 5 through 9 to determine the
531 fugacities of the remaining 5 fluid species in a graphite-bearing system (for a given value of P
532 and T). Ohmoto and Kerrick (1977), for example, determined the stability of a variety of
533 equilibria involving fluids such as H_2O and CO_2, as function of T and fO_2 at a given value of P
534 in graphite-bearing systems.

535 Lamb and Valley (1984; 1985) applied these calculations of C-O-H fluid speciation to
536 samples in which values of both fO_2 and fH_2O had been determined. If such a sample contained
537 graphite then it is possible to determine the fugacities of the remaining four fluid species, CO_2,
538 CH_4, CO, and H_2 using only equations (5) through (8). In other words, it is not necessary to
539 assume that the fluid pressure is equivalent to the lilthostatic pressure as determined using
540 mineral equilibria. In this case it would then be possible to apply equation (9) to calculate the

fluid pressure and compare this value to the lithostatic pressure. Lamb and Valley (1984; 1985) also showed that these calculations of C-O-H fluid speciation may usefully be applied to samples that do not contain graphite (i.e., not carbon saturated). In this case, if the value of fO_2 falls within the stability field of graphite then setting the value of aC = 1 will yield a minimum value of fH_2O and maximum values for CO_2 and CH_4. Furthermore, for samples in which values of both fH_2O and fO_2 were determined, but that do not contain graphite, setting aC = 1 will yield the maximum possible value of the fluid pressure via equation (9) if the value of fO_2 lies within the stability field of graphite (or diamond at higher pressures).

In this study, the computer program CalCOH (Lamb, 1987) described by Lamb and Valley (1984; 1985) was used to estimate the activities of the six fluid species listed in equations (5) through (8). A second method was also used to constrain the activities of co-existing fluid species in the C-O-H system. This method is the free energy minimization approach described by Zhang and Duan (2009), and this approach includes a seventh fluid species, C_2H_6. Addition of C_2H_6 yields a fifth reaction:

$$2C + 3H_2 = C_2H_6 \qquad (10),$$

and, in this case, equation (9) is modified by including $P_{C_2H_6}$.

These calculations, in the C-O–H system, show that the value of oxygen fugacity for our samples require an H_2O rich fluid if a lithostatically pressured C-O-H fluid is present. This result is illustrated by Figure 9 which shows the activities of four fluid species are plotted as a function of $\Delta\log(fO_2)^{FMQ}$ at aC = 1 and aC = 0.01 (Activities of CO and C_2H_6 are omitted from this figure for clarity as these are never greater than 0.001 over the range of fO_2 values shown). Regardless of the values of aC, the relative positions of three major species, CH_4, H_2O, and CO_2, are similar. CO_2 is the most abundant fluid species under relatively oxidizing condition, CH_4 becomes

predominant under reducing conditions, and H_2O is most abundant for intermediate values of fO_2. Reducing the value of carbon activity (e.g., to aC = 0.01) expands the range of fO_2 over which H_2O is the most abundant fluid species at the expense of carbon bearing species, such as CO_2 and CH_4 (Fig. 9). The extended range of H_2O predominance is accompanied with higher values of aH_2O at a given value of $\Delta\log(fO_2)^{FMQ}$ (Fig. 9). This is consistent with the previous results that show using aC = 1 for C-O-H equilibria calculation provides the minimum possible amount of H_2O in the C-O-H system at any given value of fO_2 (Lamb and Valley, 1984; 1985). The value of oxygen fugacity in each of our samples yields a fluid composition dominated by H_2O as illustrated by the value of oxygen fugacity for sample NRTP4 plotted on Figure 9. Minimum estimates of aH_2O range from 0.88 to 0.96 when estimated using Zhang and Duan (2009) and from 0.90 to 0.95 when estimated using (Lamb and Valley, 1984; 1985). These values of aH_2O are significantly greater than the values of 0.12 to 0.34 estimated using pargasite dehydration equilibrium (Table 7). The inconsistency between values of aH_2O as determined from two different methods, C-O-H equilibria and amphibole equilibrium, is also illustrated by plotting the value of aH_2O estimated from amphibole equilibrium with the value of $\Delta\log(fO_2)^{FMQ}$ for one of the samples examined in this study (NRTP4) on the diagram that illustrates the C-O-H calculations (Fig. 9). This inconsistency cannot be resolved by reducing he values of aC because aC = 1 yields the minimum values of aH_2O.

The inconsistency between the value of aH_2O as estimated from calculation of fluid speciation in the C-O-H system, and the value of aH_2O as estimated using amphibole equilibria, suggests that the assumption implied by equation (9) is not valid. In other words, the assumption that a lithostatically pressured C-O-H fluid phase must be inappropriate (Lamb and Valley, 1984; 1985). This is shown by Fig. 10, which illustrates the results of calculations in the C-O-H system

586 in fCO_2 vs. fH_2O space. This figure is plotted at a T of 720˚C and a P of 2.4 GPa, values chosen
587 based on sample NRTP4 (used as an example). The solid curve labeled 2.4 GPa (Fig. 10)
588 illustrates the composition of a C-O-H fluid in equilibrium with graphite at 2.4 GPa such that the
589 pressure of the C-O-H fluid is equivalent to the lithostatic pressure. The total pressure of a C-O-
590 H fluid must be less than the lithostatic pressure inside (below and to the left) of this curve. The
591 solid curves in this region (Fig. 10) are isopleths of fluid compositions (C-O-H only) in
592 equilibrium with graphite at pressures less than lithostatic. The dashed curves are isopleths of
593 oxygen fugacity plotted relative to FMQ. Inside the 2.4 GPa curve these fO_2 isopleths are
594 calculated at C-O-H fluid pressures less than lithostatic, while outside of this curve these
595 isopleths are calculated at 2.4 GPa for various values of $aC < 1$.

596 As noted previously, the values of aH_2O estimated from amphibole equilibria are (low
597 $aH_2O < 0.4$ for all samples), much less than the value of aH_2O estimated from calculations of
598 fluid speciation in the C-O-H system ($aH_2O > 0.9$ for all samples, see above). This suggests that
599 the assumption of fluid pressure being equivalent to the sum of the partial pressure of the fluid
600 species in the C-O-H system (equation 9) is incorrect. One possibility is that the fluid contained
601 a significant amount of non C-O-H components (e.g., N_2, S-species, or some, more exotic, fluid)
602 such that $P_{fluid} \approx P_{lith}$ and the non-C-O-H fluid pressure is relatively large (e.g., ≥ approximately
603 0.5 GPa in the case of sample NRTP4).

604 The presence of non-C-O-H fluid species cannot be ruled out, however, there is currently
605 no evidence that supports such a conclusion. Thus, our results may indicate that $P_{fluid} < P_{lith}$. It
606 has been argued that high grade ductile rocks cannot maintain open pores in which the total
607 pressure fluid pressure is significantly less that the lithostatic pressure (Walther and Orville,
608 1982; Wood and Walther, 1983; Walther and Wood, 1984). This suggests that no fluid (volatile)

609 phase was present along grain boundaries in our samples, and any OH that is present occurs
610 within hydrous or nominally anhydrous mineral phases. It might be argued that a free fluid
611 phase may be present, and that P_{fluid} may deviate from P_{lith} in high-grade rocks, during times of
612 fluid flow (Connolly and Podladchikov, 1998, 2015). In these cases, values of the fluid pressure
613 will fluctuate and, at different times may be both greater and less than lithostatic pressure.
614 However, these deviations are transient and limited in magnitude and it is not clear that these
615 short-term variations would be recorded by mineral equilibria. Thus, when mineral equilibria
616 record values of $P_{fluid} << P_{lith}$ it is likely that a free fluid was not present (fluid absence) at the
617 time of mineral equilibration (Lamb and Valley, 1984; 1985).

618 In summary, calculations of fluid speciation in the C-O-H system have typically been
619 performed with the assumption that $P_{fluid} = P_{lith}$ and, therefore, that equation (9) is routinely
620 applied when performing these calculations. However, if sufficient constraints are available,
621 such as estimates of both fH_2O and fO_2 from the same rock, it may not be necessary to make
622 this assumption. In the present case, C-O-H equilibria calculations can satisfy all mathematical
623 constraints and yield value of aH_2O consistent with those obtained from pargasite dehydration
624 equilibrium only if the fluid pressure is less than the lithostatic pressure. In the absence of
625 evidence for significant non C-O-H fluid components, these results likely indicate fluid-absent
626 condition during mineral equilibration at the estimated values of P and T.

627 ## Discussion

628 Amphiboles in the samples of this study grew relatively late as compared to other matrix
629 minerals. These textures, combined with estimates of the P and T of amphibole equilibration,
630 indicate that the amphibole grew during the exhumation stages of the Western Gneiss Region of
631 Norway. The formation of these amphiboles might be taken as evidence for the influx of H_2O-

bearing fluids during exhumation. If so, then amphibole growth could consume this H_2O and generate low values of aH_2O. This mechanism for generating reduced aH_2O is consistent with the fluid-absent conditions suggested by the calculations in the C-O-H system ($P_{fluid} < P_{lith}$). If the infiltrating fluid contained fluid species other than H_2O then the consumption of H_2O to produce amphibole could make the fluid enriched in other fluid species. In this case, the fluid must have contained a significant amount of non-C-O-H components (e.g., H_2S and N_2), as the possibility of a fluid dominated by CO_2 or CH_4 is ruled out by the C-O-H calculations at values of fO_2 that were defined for our samples (Fig. 10; Table 8).

Although we cannot rule out an external source of amphibole forming H_2O, we know of no evidence, apart from the presence of amphibole, which indicates infiltration of externally derived fluids occurred at the P-T of amphibole equilibration. The Otrøy garnet peridotites experienced pressures (e.g., 6 GPa) that are greater than the maximum stability of pargasitic mantle amphiboles (Niida and Green, 1999). Retrograde cooling and depressurization along the path shown in Figure 7 would force these rocks to traverse the amphibole stability field. Thus, if the composition of the rock included all constituents necessary for stabilizing amphibole (including H_2O-bearing NAMs) the production of a small amount of amphibole should occur under retrograde conditions. It is possible to determine if the NAMs in our samples may have contained sufficient OH to produce the amphibole now in these rocks. Sample DS0286, for example contains 1.40 % of amphibole by weight and this amphibole contains, at most, 2.14 wt% of H_2O. Thus, 100 grams of sample DS0286 has 3.00×10^{-2} grams of H_2O stored in the amphibole. If the amount of H_2O currently in amphibole is less than the maximum amount of H_2O that may have been stored in the nominally anhydrous minerals then it is theoretically possible that this internal source of H_2O was responsible for amphibole formation. The

maximum amount of H that may have been stored in olivine prior to amphibole formation would occur at the maximum P-T conditions experienced by this sample (6.5 GPa and 920 ˚C), assuming $aH_2O = 1$. Three different relations between H solubility and thermodynamic variables, such as fO_2, fH_2O, P, T and olivine composition, developed by Zhao et al. (2004), Mosenfelder et al. (2006a), and Gaetani et al. (2014), yield maximum H_2O contents of 946, 1617, or 1070 ppm by weight, respectively. After decompression and cooling to the conditions of amphibole formation (1.7 GPa, 700 ˚C, and $aH_2O = 0.23$) the olivine in this rock will contain 5, 26, or 59 ppm by weight of H_2O for these same calibrations of Zhao et al. (2004), Mosenfelder et al. (2006a), and Gaetani et al. (2014), respectively. Given that this rock contains 90.62 wt% of olivine, this mineral could have supplied from 8.52×10^{-2} to 14.42×10^{-2} grams of H_2O for 100 grams of rock. The minimum estimate of 8.52×10^{-2} grams is larger than the value of H_2O stored within amphibole present in the rock (3.00×10^{-2} grams). Given that other co-existing minerals, such as orthopyroxene, would also serve as internal source of H_2O during exhumation, it is possible that all the H required for amphibole growth was provided by co-existing NAMs even if these minerals were not saturated with H_2O at the maximum P-T conditions experienced by these rocks. In this scenario, the growth of amphibole would effectively dehydrate co-existing NAMs, and thus enhance the strength of rocks as long as the NAMs were volumetrically dominant such that they continued to control the rheology of the rock.

Olivine lattice preferred orientations from Otrøy garnet peridotites have been interpreted to indicate that these minerals were H_2O-rich (> 60 wt. ppm) at pressures > 6 GPa (Katayama et al., 2005). This evidence for the presence of significant H_2O at high pressures is consistent with NAMs as the source of H_2O in amphiboles.

677 The development of any hydrous phase, such as amphibole, could consume H_2O
678 previously present in NAMs, however, this does not rule out late-stage fluid infiltration. In some
679 cases externally derived H_2O-bearing fluids infiltrated Norwegian peridotites at relatively low
680 temperatures and pressures and this resulted in the production of chlorite and serpentine
681 (Kostenko et al., 2002).

682 In summary, values of aH_2O, as estimated using amphibole dehydration equilibria in the
683 samples examined in this study, range from 0.12 to 0.34. The presence of amphibole in mantle
684 rocks, therefore, does not require the presence of H_2O-rich fluids. Value of fO_2 estimated for
685 these samples range from approximately 1.6 to 2.2 log units below the FMQ oxygen buffer.
686 These fO_2 estimates are within the range of values determined for the mantle, which are often
687 within +1 to -2 log units of FMQ (Bryndzia and Wood, 1990; Wood et al., 1990; Ionov and
688 Wood, 1992; Woodland and Koch, 2003). Although some studies have noted a correlation
689 between elevated values of oxygen fugacity and the presence of amphibole in mantle samples
690 (Mattioli et al., 1989; Bryndzia and Wood, 1990; Wood et al., 1990), the samples described here
691 equilibrated under relatively reducing conditions. These values of oxygen fugacity, in
692 combination with calculation of fluid speciation in the C-O-H system, rule out the presence of a
693 fluid dominated by either CO_2 or CH_4. Thus, if a lithostatically-pressured fluid were present, it
694 must have had relatively low concentrations of H_2O, CO_2, and/or CH_4 and either a more exotic
695 fluid was dominant (e.g., N_2), or the rocks equilibrated in the absence of a free fluid phase. In the
696 later case, amphibole growth could consume H_2O and result in fluid absence if relatively small
697 amounts of H_2O were infiltrated the rocks. However, fluid infiltration at the P-T of mineral
698 equilibration is not required as H_2O could have been stored in NAMs at high P-T and this H_2O
699 could be consumed by amphibole during retrograde depressurization.
700

Acknowledgements

We thank Dr. Ray Guillemette who provided invaluable assistance with the electron microprobe analyses. Dirk Spengler is thanked for providing some of the samples for this study. Evan Smith is acknowledged for his contribution to the data included in this study (electron microprobe analyses on selected minerals from some of the samples). Support for this research was provided, in part, by a grant awarded to W. Lamb and R. Popp from the Texas Advanced Research Program. This paper benefitted from input by Costanza Bonadiman and anonymous reviewers.

711 References
712
713 Agrinier, P., Mevel, C., Bosch, D., and Javoy, M. (1993) Metasomatic hydrous fluids in
714 amphibole peridotites from Zabargad Island, Red Sea. Earth and Planet. Sci Lett., 120,
715 187-205.

716 Asimow, P.D., and Ghiorso, M.S. (1998) Algorithmic modifications extending MELTS to
717 calculate subsolidus phase relations. American Mineralogist, 83, 1127-1132.

718 Bai, Q., and Kohlstedt, D.L. (1992) Sustantial hydrogen solubility in olivine and implications for
719 water storage in the mantle. Nature, 357, p. 672-674.

720 Bai, Q., and Kohlstedt, H.L. (1993) Effects of chemical environment on the solublity and
721 incorporation mechanism for hydrogen in olivine. Physics and Chemistry of Minerals, 19,
722 460-471.

723 Bell, D.R., Rossman, G.R., Maldener, J., Endisch, D., and Rauch, F. (2003) Hydroxide in
724 olivine: A quantitative determination of the absolute amount and calibration of the IR
725 spectrum. Journal of Geophysical Research-Solid Earth, 108.

726 Bonadiman, C., Nazzareni, S., Coltorti, M., Comodi, P., Giuli, G., and Faccini, B. (2014) Crystal
727 chemistry of amphiboles: implications for oxygen fugacity and water activity in
728 lithospheric mantle beneath Victoria Land, Antarctica. Contributions to Mineralogy and
729 Petrology, 167.

730 Brey, G.P., and Köhler, T. (1990) Geothermobarometry in Four-phase Lherzolites II. New
731 Thermobarometers, and Practical Assessment of Existing Thermobarometers. Jour
732 Petrology, 31, 1353-1378.

733 Brueckner, H.K., Carswell, D.A., and Griffin, W.L. (2002) Paleozoic Diamonds Within a
734 Precambrian Peridotite Lens in UHP Gneisses of the Norwegian Caledonides. Earth and
735 Planetary Science Letters, 203, 805-816.

736 Bryndzia, L.T., and Wood, B.J. (1990) Oxygen Thermobarometry of Abyssal Spinel Peridotites -
737 the Redox State and C-O-H Volatile Composition of the Earths Sub-Oceanic Upper
738 Mantle. American Journal of Science, 290, 1093-1116.

739 Canil, D., and O'Neill, H.S.C. (1996) Distribution of ferric iron in some upper-mantle
740 assemblages. Journal of Petrology, 37, 609-635.

741 Carswell, D.A. (1986) The Metamorphic Evolution of Mg-Cr Type Norwegian Garnet
742 Peridotites. Lithos, 19, 279-297.

743 Carswell, D.A., and Van Roermund, H.L.M. (2005) On multi-phase mineral inclusions
744 associated with microdiamond formation in mantle-derived peridotite lens at Bardane on
745 Fjortoft, west Norway. European Journal of Mineralogy, 17, 31-42.

Coltorti, M., Beccaluva, L., Bonadiman, C., Faccini, B., Ntaflos, T., and Siena, F. (2004) Amphibole genesis via metasomatic reaction with clinopyroxene in mantle xenoliths from Victoria Land, Antarctica. Lithos, 75, 115-139.

Connolly, J.A.D., and Cesare, B. (1993) C-O-H-S Fluid Composition and Oxygen Fugacity in Graphitic Metapelites. Journal of Metamorphic Geology, 11, 379-388.

Connolly, J.A.D., and Podladchikov, Y.Y. (1998) Compaction-driven fluid flow in viscoelastic rock. Geodinamica Acta, 11, 55-84.

-. (2015) An analytical solution for solitary porosity waves: dynamic permeability and fluidization of nonlinear viscous and viscoplastic rock. Geofluids, 15, 269-292.

Dale, J., Powell, R., White, R.W., Elmer, F.L., and Holland, T.J.B. (2005) A thermodynamic model for Ca-Na clinoamphiboles in Na2O-CaO-FeO-MgO-Al2O3-SiO2-H2O-O for petrological calculations. Journal of Metamorphic Geology, 23, 771-791.

Demouchy, S., and Mackwell, S. (2006) Mechanisms of hydrogen incorporation and diffusion in iron-bearing olivine. Physics and Chemistry of Minerals, 33, 347-355.

Drury, M.R., Van Roermund, H.L.M., Carswell, D.A., De Smet, J.H., Van den Berg, A.P., and Vlaar, N.J. (2001) Emplacement of deep upper-mantle rocks into cratonic lithosphere by convection and diapiric upwelling. Journal of Petrology, 42, 131-140.

Dyar, M.D., Mackwell, S.J., Mcguire, A.V., Cross, L.R., and Robertson, J.D. (1993) Crystal-Chemistry of Fe^{3+} and H^{+} in Mantle Kaersutite - Implications for Mantle Metasomatism. American Mineralogist, 78, 968-979.

French, B.M. (1966) Some Geological Implications of Equilibrium between Graphite and a C - H - O Gas Phase at High Temperatures and Pressures. Reviews of Geophysics, 4, 223-&.

Gaetani, G.A., O'Leary, J.A., Koga, K.T., Hauri, E.H., Rose-Koga, E.F., and Monteleone, B.D. (2014) Hydration of mantle olivine under variable water and oxygen fugacity conditions. Contributions to Mineralogy and Petrology, 167.

Gentili, S., Bonadiman, C., Biagioni, C., Comodi, P., Coltorti, M., Zucchini, A., and Ottolini, L. (2015) Oxo-amphiboles in mantle xenoliths: evidence for H2O-rich melt interacting with the lithospheric mantle of Harrow Peaks (Northern Victoria Land, Antarctica). Mineralogy and Petrology, 109, 741-759.

Ghiorso, M.S., and Evans, B.W. (2002) Thermodynamics of the amphiboles: Ca-Mg-Fe2+ quadrilateral. American Mineralogist, 87, 79-98.

Ghiorso, M.S., and Sack, R.O. (1995) Chemical Mass-Transfer in Magmatic Processes .4. A Revised and Internally Consistent Thermodynamic Model for the Interpolation and Extrapolation of Liquid-Solid Equilibria in Magmatic Systems at Elevated-Temperatures and Pressures. Contributions to Mineralogy and Petrology, 119, 197-212.

781 Green, D.H. (1973) Experimental Melting Studies on a Model Upper Mantle Composition at
782 High-Pressure under Water-Saturated and Water-Undersaturated Conditions. Earth and
783 Planetary Science Letters, 19, 37-53.

784 -. (2015) Experimental petrology of peridotites, including effects of water and carbon on melting
785 in the Earth's upper mantle. Physics and Chemistry of Minerals, 42, 95-122.

786 Green, D.H., Hibberson, W.O., Rosenthal, A., Kovacs, I., Yaxley, G.M., Falloon, T.J., and
787 Brink, F. (2014) Experimental Study of the Influence of Water on Melting and Phase
788 Assemblages in the Upper Mantle. Journal of Petrology, 55, 2067-2096.

789 Green, D.H., and Ringwood, A.E. (1970) Mineralogy of peridotitic compositions under upper
790 mantle conditions. Phys Earth Planet Int 3, 359-371.

791 Grütter, H., Latti, D., and Menzies, A. (2006) Cr-saturation arrays in concentrate garnet
792 compositions from kimberlite and their use in mantle barometry. Journal of Petrology,
793 47, 801-820.

794 Grütter, H.S. (2009) Pyroxene xenocryst geotherms: Techniques and application. Lithos, 112,
795 1167-1178.

796 Hauri, E.H., Gaetani, G.A., and Green, T.H. (2006) Partitioning of water during melting of the
797 Earth's upper mantle at H2O-undersaturated conditions. Earth and Planetary Science
798 Letters, 248, 715-734.

799 Hirth, G., and Kohlstedt, D.L. (1996) Water in the oceanic upper mantle: implication for
800 rheology, melt extraction and the evolution of the lithosphere. Earth and Planetary
801 Science Letters, 144, 93-108.

802 Ingrin, J., and Skogby, H. (2000) Hydrogen in nominally anhydrous upper-mantle minerals:
803 concentration levels and implications. European Journal of Mineralogy, 12, 543-570.

804 Ionov, D.A., Bodinier, J.L., Mukasa, S.B., and Zanetti, A. (2002) Mechanisms and sources of
805 mantle metasomatism: Major and trace element compositions of peridotite xenoliths from
806 Spitsbergen in the context of numerical modelling. Journal of Petrology, 43, 2219-2259.

807 Ionov, D.A., and Hofmann, A.W. (1995) Nb-Ta-Rich Mantle Amphiboles and Micas -
808 Implications for Subduction-Related Metasomatic Trace-Element Fractionations. Earth
809 and Planetary Science Letters, 131, 341-356.

810 Ionov, D.A., and Wood, B.J. (1992) The Oxidation-State of Subcontinental Mantle - Oxygen
811 Thermobarometry of Mantle Xenoliths from Central-Asia. Contributions to Mineralogy
812 and Petrology, 111, 179-193.

813 Jung, H., and Karato, S. (2001) Water-induced fabric transitions in olivine. Science, 293, 1460-
814 1463.

Jung, H., Katayama, I., Jiang, Z., Hiraga, I., and Karato, S. (2006) Effect of water and stress on the lattice-preferred orientation of olivine. Tectonophysics, 421, 1-22.

Karato, S., and Jung, H. (1998) Water, partial melting and the origin of the seismic low velocity and high attenuation zone in the upper mantle. Earth and Planetary Science Letters, 157, 193-207.

Katayama, I., Karato, S.I., and Brandon, M. (2005) Evidence of high water content in the deep upper mantle inferred from deformation microstructures. Geology, 33, 613-616.

Klemme, S. (2004) The influence of Cr on the garnet-spinel transition in the Earth's mantle: experiments in the system MgO-Cr2O3-SiO2 and thermodynamic modelling. Lithos, 77, 639-646.

Kostenko, O., Jamtveit, B., Austrheim, H., Pollok, K., and Putnis, C. (2002) The mechanism of fluid infiltration in peridotites at Almklovdalen, western Norway. Geofluids, 2, 203-215.

Kushiro, I. (1972) Effect of Water on Composition of Magmas Formed at High-Pressures. Journal of Petrology, 13, 311-&.

Lamb, W.M. (1987) Metamorphic fluids and granulite genesis. Ph.D., Dept. of Geology and Geophysics, University of Wisconsin, 234 pages.

Lamb, W.M., and Popp, R.K. (2009) Amphibole equilibria in mantle rocks: Determining values of mantle aH_2O and implications for mantle H_2O contents. American Mineralogist, 94, 41-52.

Lamb, W.M., and Valley, J.W. (1984) Metamorphism of Reduced Granulites in Low-CO_2 Vapor-Free Environment. Nature, 312, 56-58.

Lamb, W.M., and Valley, J.W. (1985) C-O-H fluid calculations and granulite genesis. In Tobi, A., and Touret, J., Eds. The deep proterozoic crust in the North Atlantic Provinces, 119-131. Reidel Pub.

Long, M.D., and van der Hilst, R.D. (2005) Upper mantle anisotropy beneath Japan from shear wave splitting. Physics of the Earth and Planetary Interiors, 151, 206-222.

Mainprice, D., Tommasi, A., Couvy, H., Cordier, P., and Frost, D.J. (2005) Pressure sensitivity of olivine slip systems and seismic anisotropy of Earth's upper mantle. Nature, 433, 731-733.

Maldener, J., Hosch, A., Langer, K., and Rauch, F. (2003) Hydrogen in some natural garnets studied by nuclear reaction analysis and vibrational spectroscopy. Physics and Chemistry of Minerals, 30, 337-344.

Mattioli, G.S., Baker, M.B., Rutter, M.J., and Stolper, E.M. (1989) Upper Mantle Oxygen Fugacity and Its Relationship to Metasomatism. Journal of Geology, 97, 521-536.

McCammon, C., and Kopylova, M.G. (2004) A redox profile of the Slave mantle and oxygen fugacity control in the cratonic mantle. Contributions to Mineralogy and Petrology, 148, 55-68.

Medaris, L.G. (1984) A geothermobarometric investigation of garnet peridotites in the western gneiss region of Norway. Contributions to Mineralogy and Petrology, 87, 72-86.

Mei, S., and Kohlstedt, D.L. (2000a) Influence of water on plastic deformation of olivine aggregates 2. Dislocation creep regime. Journal of Geophysical Research, 105, 21,471 - 21,481.

-. (2000b) Influence of water on plastic deformation of olivine aggregates 1. Diffusion creep regime. Journal of Geophysical Research, 105, 21,457-21,469.

Moresi, L., and Solomatov, V. (1998) Mantle convection with a brittle lithosphere: thoughts on the global tectonic styles of the Earth and Venus. Geophysical Journal International, 133, 669-682.

Mosenfelder, J.L., Deligne, N.I., Asimow, P.D., and Rossman, G.R. (2006a) Hydrogen incorporation in olivine from 2-12 GPa. American Mineralogist, 91, 285-294.

Mosenfelder, J.L., Sharp, T.G., Asimow, P.D., and Rossman, G.R. (2006b) Hydrogen Incorporation in Natural Mantle Olivines. Earths Deep Water Cycle, 168, 45-56.

Nakajima, J., and Hasegawa, A. (2004) Shear-wave polarization anisotropy and subduction-induced flow in the mantle wedge of northeastern Japan. Earth and Planetary Science Letters, 225, 365-377.

Nehru, C.E., and Wyllie, P.J. (1975) Compositions of Glasses from St Pauls Peridotite Partially Melted at 20 Kilobars. Journal of Geology, 83, 455-471.

Nicholls, I.A., and Ringwood, A.E. (1972) Production of Silica-Saturated Tholeiitic Magmas in Island Arcs. Earth and Planetary Science Letters, 17, 243-246.

Nicholls, L.A., and Ringwood, A.E. (1973) Effect of Water on Olivine Stability in Tholeiites and Production of Silica-Saturated Magmas in Island-Arc Environment. Journal of Geology, 81, 285-300.

Nickel, K.G., and Green, D.H. (1985) Empirical Geothermobarometry for Garnet Peridotites and Implications for the Nature of the Lithosphere, Kimberlites and Diamonds. Earth and Planetary Science Letters, 73, 158-170.

Niida, K., and Green, D.H. (1999) Stability and chemical composition of pargasitic amphibole in MORB pyrolite under upper mantle conditions. Contributions to Mineralogy and Petrology, 135, 18-40.

Nimis, P., and Grütter, H. (2010) Internally consistent geothermometers for garnet peridotites and pyroxenites. Contributions to Mineralogy and Petrology, 159, 411-427.

884 Nimis, P., and Taylor, W.R. (2000) Single clinopyroxene thermobarometry for garnet peridotites.
885 Part I. Calibration and testing of a Cr-in-Cpx barometer and an enstatite-in-Cpx
886 thermometer. Contributions to Mineralogy and Petrology, 139, 541-554.

887 O'Neill, H.S.C., and Wood, B.J. (1979) Experimental-Study of Fe-Mg Partitioning between
888 Garnet and Olivine and Its Calibration as a Geothermometer. Contributions to
889 Mineralogy and Petrology, 70, 59-70.

890 O'Reilly, S.Y., and Griffin, W.L. (2013) Mantle Metasomatism. In Harlov, D.E., and Austrheim,
891 H., Eds. Metasomatism and the Chemical Transformation of Rock, 471-533. Springer,
892 Berlin.

893 Obata, M., and Ozawa, K. (2011) Topotaxic relationships between spinel and pyroxene in
894 kelyphite after garnet in mantle-derived peridotites and their implications to reaction
895 mechanism and kinetics. Mineralogy and Petrology, 101, 217-224.

896 Ohmoto, H., and Kerrick, D. (1977) Devolatilization Equilibria in Graphitic Systems. American
897 Journal of Science, 277, 1013-1044.

898 Ohuchi, T., Kawazoe, T., Nishihara, Y., and Irifune, T. (2012) Change of olivine a-axis
899 alignment induced by water: Origin of seismic anisotropy in subduction zones. Earth and
900 Planetary Science Letters, 317, 111-119.

901 Oxburgh, E.R. (1964) Upper Mantle Inhomogeneity and the Low Velocity Zone. Geophysical
902 Journal of the Royal Astronomical Society, 8, 456-462.

903 Peslier, A.H. (2010) A review of water contents of nominally anhydrous natural minerals in the
904 mantles of Earth, Mars and the Moon. Journal of Volcanology and Geothermal Research,
905 197, 239-258.

906 Peslier, A.H., and Luhr, J.F. (2005) Water contents in anhydrous minerals from the upper-mantle
907 (peridotites and eclogites). Geochimica Et Cosmochimica Acta, 69, A745-A745.

908 Peslier, A.H., Woodland, A.B., Bell, D.R., and Lazarov, M. (2010) Olivine water contents in the
909 continental lithosphere and the longevity of cratons. Nature, 467, 78-U108.

910 Popp, R.K., and Bryndzia, L.T. (1992) Statistical-Analysis of Fe^{3+}, Ti, and Oh in Kaersutite from
911 Alkalic Igneous Rocks and Mafic Mantle Xenoliths. American Mineralogist, 77, 1250-
912 1257.

913 Popp, R.K., Hibbert, H.A., and Lamb, W.M. (2006) Oxy-amphibole equilibria in Ti-bearing
914 calcic amphiboles: Experimental investigation and petrologic implications for mantle-
915 derived amphiboles. American Mineralogist, 91, 716-716.

916 Popp, R.K., Virgo, D., Yoder, H.S., Hoering, T.C., and Phillips, M.W. (1995) An Experimental-
917 Study of Phase-Equilibria and Fe Oxy-Component in Kaersutitic Amphibole -
918 Implications for the fH_2 and aH_2O in the Upper-Mantle. American Mineralogist, 80, 534-
919 548.

Powell, W., Zhang, M., O'Reilly, S.Y., and Tiepolo, M. (2004) Mantle amphibole trace-element and isotopic signatures trace multiple metasomatic episodes in lithospheric mantle, western Victoria, Australia. Lithos, 75, 141-171.

Rauch, M., and Keppler, H. (2002) Water solubility in orthopyroxene. Contributions to Mineralogy and Petrology, 143, 525-536.

Roberts, D., and Gee, D. (1985) An introduction to the structure of the Scandinavian Caledonides. In Gee, D., and Sturt, B., Eds. The Caledonide Orogen-Scandinavia and related areas, 55-68. John Wiley & Sons, Chichester.

Skogby, H. (1994) OH Incorporation in Synthetic Clinopyroxene. American Mineralogist, 79, 240-249.

Smith, D.C. (1984) Coesite in Clinopyroxene in the Caledonides and Its Implications for Geodynamics. Nature, 310, 641-644.

Solomatov, V.S. (1995) Scaling of Temperature-Dependent and Stress-Dependent Viscosity Convection. Physics of Fluids, 7, 266-274.

Spengler, D., Brueckner, H.K., van Roermund, H.L.M., Drury, M.R., and Mason, P.R.D. (2009) Long-lived, cold burial of Baltica to 200 km depth. Earth and Planetary Science Letters, 281, 27-35.

Spengler, D., van Roermund, H.L.M., Drury, M.R., Ottolini, L., Mason, P.R.D., and Davies, G.R. (2006) Deep origin and hot melting of an Archaean orogenic peridotite massif in Norway. Nature, 440, 913-917.

Stalder, R., Klemme, S., Ludwig, T., and Skogby, H. (2005) Hydrogen incorporation in orthopyroxene: interaction of different trivalent cations. Contributions to Mineralogy and Petrology, 150, 473-485.

Stalder, R., and Ludwig, T. (2007) OH incorporation in synthetic diopside. European Journal of Mineralogy, 19, 373-380.

Sundvall, R., and Skogby, H. (2011) Hydrogen defect saturation in natural pyroxene. Physics and Chemistry of Minerals, 38, 335-344.

Tackley, P.J. (1998) Self-consistent generation of tectonic plates in three-dimensional mantle convection. Earth and Planetary Science Letters, 157, 9-22.

Taylor, W.R. (1998) An experimental test of some geothermometer and geobarometer formulations for upper manlte peridotites with application to the thermobarometry of fertile lherzolite and garnet websterite. N. Jb. Mineral. Abh., 173, 381-408.

van Roermund, H. (2009) Mantle-wedge garnet peridotites from the northernmost ultra-high pressure domain of the Western Gneiss Region, SW Norway. European Journal of Mineralogy, 21, 1085-1096.

Van Roermund, H.L.M., Carswell, D.A., Drury, M.R., and Heijboer, T.C. (2002) Microdiamonds in a megacrystic garnet websterite pod from Bardane on the island of Fjørtoft, western Norway: Evidence for diamond formation in mantle rocks during deep continental subduction. Geology, 30, 959-962.

Vannucci, R., Piccardo, G.B., Rivalenti, G., Zanetti, A., Rampone, E., Ottolini, L., Oberti, R., Mazzucchelli, M., and Bottazzi, P. (1995) Origin of Lree-Depleted Amphiboles in the Subcontinental Mantle. Geochimica Et Cosmochimica Acta, 59, 1763-1771.

Voigt, M., and von der Handt, A. (2011) Influence of subsolidus processes on the chromium number in spinel in ultramafic rocks. Contributions to Mineralogy and Petrology, 162, 675-689.

Vrijmoed, J.C., Van Roermund, H.L.M., and Davies, G.R. (2006) Evidence for diamond-grade ultra-high pressure metamorphism and fluid interaction in the Svartberget Fe-Ti garnet peridotite-websterite body, Western Gneiss Region, Norway. Mineralogy and Petrology, 88, 381-405.

Walther, J.V., and Orville, P.M. (1982) Volatile Production and Transport in Regional Metamorphism. Contributions to Mineralogy and Petrology, 79, 252-257.

Walther, J.V., and Wood, B.J. (1984) Rate and Mechanism in Prograde Metamorphism. Contributions to Mineralogy and Petrology, 88, 246-259.

Warren, J.M., and Hauri, E.H. (2014) Pyroxenes as tracers of mantle water variations. Journal of Geophysical Research-Solid Earth, 119, 1851-1881.

Wood, B.J. (1990) An Experimental Test of the Spinel Peridotite Oxygen Barometer. Journal of Geophysical Research-Solid Earth and Planets, 95, 15845-15851.

Wood, B.J., Bryndzia, L.T., and Johnson, K.E. (1990) Mantle Oxidation-State and Its Relationship to Tectonic Environment and Fluid Speciation. Science, 248, 337-345.

Wood, B.J., and Virgo, D. (1989) Upper mantle oxidation state: Ferric iron contents of lherzolite spinels by ^{57}Fe Mossbauer spectroscopy and resultant oxygen fugacities. Geochimica et Cosmochimica Acta, 53, 1277-1291.

Wood, B.J., and Walther, J.V. (1983) Rates of Hydrothermal Reactions. Science, 222, 413-415.

Woodland, A.B., and Koch, M. (2003) Variation in oxygen fugacity with depth in the upper mantle beneath the Kaapvaal craton, Southern Africa. Earth and Planetary Science Letters, 214, 295-310.

Woodland, A.B., Kornprobst, J., and Wood, B.J. (1992) Oxygen Thermobarometry of Orogenic Lherzolite Massifs. Journal of Petrology, 33, 203-230.

988 Wu, C.M., and Zhao, G.C. (2007) A recalibration of the garnet-olivine geothermometer and a
989 new geobarometer for garnet peridotites and garnet-olivine-plagioclase-bearing
990 granulites. Journal of Metamorphic Geology, 25, 497-505.

991 Zhang, C., and Duan, Z.H. (2009) A model for C-O-H fluid in the Earth's mantle. Geochimica Et
992 Cosmochimica Acta, 73, 2089-2102.

993 Zhao, Y.-H., Ginsberg, S.B., and Kohlstedt, D.L. (2004) Solubility of hydrogen in olivine:
994 dependence on temperature and iron content. Contributions of Mineralogy and Petrology,
995 147, 155-161.
996
997
998
999

Table 1: Microprobe analyses (wt%) and normalized cations per formula unit of garnet in DS0286 (Distances are from the rim represented by the 1st analysis)

	Rim	717µm	1544µm	1956µm	2505µm	2897µm	3468µm	Rim 4022µm
SiO_2	41.37	41.30	41.25	41.29	41.26	41.57	41.45	41.43
Al_2O_3	22.22	22.15	22.10	22.10	22.09	22.19	22.10	22.05
TiO_2	BDL	BDL	BDL	0.05	BDL	BDL	BDL	BDL
Cr_2O_3	2.81	2.73	2.64	2.78	2.82	2.85	2.86	3.10
FeO	8.97	9.47	9.12	9.59	9.15	9.33	9.34	9.13
MnO	0.52	0.53	0.49	0.45	0.42	0.42	0.47	0.55
MgO	19.19	19.03	18.81	19.13	19.07	19.07	19.09	19.39
CaO	4.97	5.02	4.94	5.06	4.99	5.03	4.91	4.60
Sum	100.04	100.23	99.34	100.43	99.80	100.46	100.22	100.25
Formulae normalized to eight cations								
$Si^{(IV)}$	2.964	2.958	2.979	2.952	2.965	2.971	2.969	2.964
$Al^{(IV)}$	0.036	0.042	0.021	0.048	0.035	0.029	0.031	0.036
$Al^{(VI)}$	1.841	1.828	1.861	1.813	1.837	1.839	1.835	1.824
Ti	-	-	-	0.003	-	-	-	-
Cr	0.159	0.155	0.151	0.157	0.160	0.161	0.162	0.175
Fe^{3+}	0.036	0.058	0.009	0.072	0.038	0.029	0.034	0.036
Fe^{2+}	0.501	0.509	0.542	0.501	0.512	0.529	0.525	0.510
Mn	0.032	0.032	0.030	0.027	0.026	0.025	0.029	0.033
Mg	2.050	2.032	2.025	2.039	2.043	2.031	2.038	2.068
Ca	0.382	0.385	0.382	0.388	0.384	0.385	0.377	0.353
Sum	8.000	8.000	8.000	8.000	8.000	8.000	8.000	8.000

BDL, concentration below the detection limit; All data are available in the electronic appendix

Table 2: Microprobe analyses (wt%) and normalized cations per formula unit of matrix orthopyroxene, orthopyroxene rim surrounding the kelyphite (COR), and the kelyphite in NRTP4

	Matrix orthopyroxene		**COR**		**Orthopyroxene within kelyphite**	
	Core	**Rim**	**Adjacent to kelyphite**	**Adjacent to the matrix**	**Adjacent to garnet**	**Adjacent to the matrix**
SiO_2	58.52	57.80	56.32	57.36	50.04	56.04
Al_2O_3	0.64	1.00	2.51	1.10	10.58	2.69
TiO_2	BDL	BDL	BDL	BDL	BDL	BDL
Cr_2O_3	0.13	0.17	0.13	BDL	1.11	0.23
FeO	5.41	6.03	6.22	5.89	6.58	6.28
MnO	0.10	0.19	0.00	0.26	0.21	0.27
MgO	36.15	35.47	33.61	33.99	32.08	33.64
CaO	0.15	0.18	0.22	0.19	0.15	0.21
NiO	BDL	BDL	BDL	0.11	BDL	BDL
Na_2O	BDL	BDL	BDL	BDL	BDL	BDL
K_2O	BDL	BDL	BDL	BDL	BDL	BDL
Sum	101.11	100.83	99.01	98.90	100.74	99.35
Formulae normalized to four cations						
$Si^{(IV)}$	1.983	1.970	1.960	1.999	1.710	1.945
$Al^{(IV)}$	0.017	0.030	0.040	0.001	0.290	0.055
$Al^{(VI)}$	0.009	0.010	0.063	0.044	0.136	0.055
Cr	0.003	0.005	0.004	-	0.030	0.006
Fe^{3+}	0.005	0.016	0.000	0.000	0.124	0.000
Fe^{2+}	0.149	0.156	0.181	0.172	0.064	0.182
Mn	0.003	0.005	0.000	0.008	0.006	0.008
Mg	1.826	1.802	1.744	1.766	1.634	1.741
Ca	0.005	0.007	0.008	0.007	0.005	0.008
Ni	-	-	-	0.003	-	-
Sum	4.000	4.000	4.000	4.000	4.000	4.000

BDL, concentration below the detection limit; All data are available in the electronic appendix

Table 3: Microprobe analyses (wt%) of matrix amphibole in close proximity to kelyphite in NRTP4 (Rim is adjacent to the matrix, distance from Rim* are given for subsequent analyses, and Rim** is adjacent to kelyphite)*

	Rim*	**98µm**	**661µm**	**907µm**	**1048µm**	**Rim****
SiO_2	45.46	45.81	46.23	45.23	44.93	45.17
Al_2O_3	13.59	13.29	12.89	13.09	13.86	14.79
TiO_2	0.30	0.37	0.35	0.28	0.36	0.14
Cr_2O_3	1.98	2.12	2.15	2.30	1.98	1.47
FeO	2.34	2.35	2.33	2.86	2.94	2.73
MnO	BDL	BDL	BDL	BDL	BDL	BDL
MgO	18.48	18.83	18.76	18.59	18.69	17.51
CaO	12.39	12.34	12.33	11.89	11.94	12.31
NiO	BDL	BDL	BDL	BDL	BDL	BDL
Na_2O	2.53	2.37	2.36	2.28	2.32	2.23
K_2O	0.06	0.12	0.09	0.08	BDL	BDL
F	BDL	BDL	BDL	BDL	BDL	BDL
Cl	BDL	BDL	BDL	BDL	BDL	BDL
H_2O	2.08	2.12	2.09	2.04	2.09	2.10
SUM	99.21	99.70	99.58	98.63	99.11	98.44
O=F	0.03	0.01	0.03	0.06	0.02	0.01
O=Cl	0.01	0.01	0.01	0.01	0.01	0.01
SUM	99.16	99.68	99.54	98.56	99.09	98.43

BDL, concentration below the detection limit; All data are available in the electronic appendix

Table 4: Microprobe analyses (wt%) of matrix amphibole replacing matrix clinopyroxene in NRTP4 (Distances are from the rim adjacent to the 1st analysis)

	Rim	127µm	250µm	394µm	Rim 553µm
SiO_2	46.12	45.27	45.92	45.57	45.89
Al_2O_3	12.97	11.86	12.95	12.90	12.92
TiO_2	0.38	0.31	0.36	0.35	0.34
Cr_2O_3	1.96	2.06	2.04	2.12	1.95
FeO	2.58	3.28	2.28	2.40	2.56
MnO	BDL	BDL	BDL	BDL	BDL
MgO	19.60	20.47	19.48	19.48	19.74
CaO	12.57	11.31	12.45	12.34	12.22
NiO	BDL	BDL	BDL	BDL	BDL
Na_2O	2.68	2.43	2.55	2.65	2.65
K_2O	0.08	0.07	0.20	0.16	0.07
F	BDL	BDL	BDL	BDL	BDL
Cl	BDL	BDL	BDL	BDL	BDL
H_2O	2.15	2.10	2.13	2.13	2.14
SUM	101.09	99.15	100.38	100.10	100.47
O=F	0.00	0.00	0.00	0.00	0.00
O=Cl	0.01	0.01	0.01	0.01	0.01
SUM	101.08	99.14	100.36	100.09	100.46

BDL, concentration below the detection limit; All data are available in the electronic appendix

Table 5: Microprobe analyses (wt%) and normalized cations per formula unit of matrix amphibole and fine-grained amphiboles within the kelyphite from NRTP4

	Matrix amphibole		Amphibole within the kelyphite	
	Core	**Rim (Adjacent to kelyphite)**	**Adjacent to garnet**	**Adjacent to the matrix**
SiO_2	45.35	45.17	44.61	44.90
Al_2O_3	13.15	14.79	14.64	15.71
TiO_2	0.39	0.14	0.28	0.21
Cr_2O_3	2.18	1.47	1.89	1.41
FeO	2.31	2.73	2.92	2.92
MnO	BDL	BDL	0.07	0.08
MgO	18.89	17.51	18.34	18.33
CaO	12.52	12.31	12.50	12.51
NiO	BDL	BDL	0.05	0.09
Na_2O	2.29	2.23	2.24	2.24
K_2O	0.29	BDL	0.05	0.02
F	BDL	BDL	0.01	BDL
Cl	BDL	BDL	0.03	0.02
H_2O	2.09	2.10	2.11	2.15
Sum	99.44	98.44	99.73	100.57
O=F	0.03	0.01	0.01	0.00
O=Cl	0.01	0.01	0.01	0.01
SUM	99.40	98.43	99.72	100.57
Average of normalized formulae using the empirical relations of Ox = Ti+Fe and Ox = $(Fe^{3+}/0.93)$-0.65591-(F#+Cl#)+$((Ti+AlM_{123})/0.93)$,				
$Si^{(IV)}$	6.403	6.434	6.299	6.291
$Al^{(IV)}$	1.597	1.566	1.701	1.709
$Ti^{(M123)}$	0.042	0.015	0.030	0.030
$Al^{(M123)}$	0.591	0.917	0.735	0.740
$Cr^{(M123)}$	0.243	0.166	0.211	0.233
$Fe^{2+(M123)}$	0.149	0.185	0.158	0.159
$Mg^{(M123)}$	3.975	3.717	3.860	3.828
$Mn^{(M123)}$	-	-	0.000	0.000
$Ni^{(M123)}$	-	-	0.006	0.010
$Mg^{(M4)}$	0.000	0.000	0.000	0.000
$Fe^{2+(M4)}$	0.124	0.140	0.187	0.176
$Mn^{(M4)}$	-	-	0.008	0.007
$Ca^{(M4)}$	1.876	1.839	1.805	1.817
$Na^{(M4)}$	0.000	0.021	0.000	0.000
$Ca^{(A)}$	0.017	0.039	0.086	0.064
$Na^{(A)}$	0.626	0.596	0.613	0.649
$K^{(A)}$	0.052	-	0.009	0.005
Vac	0.306	0.365	0.291	0.282
F	-	-	0.005	-
Cl	-	-	0.007	0.005
O	0.032	0.199	0.099	0.106
OH	1.968	1.801	1.889	1.889

BDL, concentration below the detection limit; All data are available in the electronic appendix

1036
1037
1038
1039 *Table 6: Pressure and temperature estimates based on three different combinations of*
1040 *geothermometers in conjunction with the geobarometer of Nickel and Green (1985)*

Sample	Taylor(98) (˚C & kbar)	Corrected Brey and Köhler(09) (˚C & kbar)	Nimis and Grutter(09) (˚C & kbar)
NRTP4	720, 24	660, 21	670, 21
DS0260	780, 27	690, 24	810, 28
DS0286	700, 17	680, 16	770, 20
NUM9a	740, 27	650, 22	670, 23

1041
1042
1043
1044

Table 7: Activities of mineral end members in natural phases, H_2O activities estimated from amphibole dehydration equilibrium, and oxygen fugacity estimates

Sample	aEn	aDi	aJd	aFo	aSp	aParg	aH_2O	$\Delta\log(fO_2)^{FMQ}$
NRTP4	0.85	0.91	0.01	0.85	0.49	0.44	0.34	-2.18
DS0260	0.84	0.88	0.04	0.83	0.45	0.52	0.26	-3.19
DS0286	0.85	0.90	0.01	0.85	0.51	0.47	0.23	-1.98
NUM9a	0.88	0.85	0.07	0.87	0.46	0.53	0.12	-1.76

En - enstatite, Di - diopside, Jd - jadeite, Fo - forsterite, Sp - spinel, and Parg - pargasite.

Figure Captions:

Fig. 1 Location maps of the Western Gneiss Region of Norway. A box in the left map (Regional map of Norway) indicates the location of the Western Gneiss Region of Norway, which is magnified on the right. The location of Otrøy Island and the distribution of garnet peridotites are indicated by circles and triangles. A, B, and C refer to northern, central, and southern ultra-high pressure domains (outlined by black lines). Modified from Van Roermund (2009).

Fig. 2 Optical micrographs illustrating typical mineralogies and textures. (a) Optical micrograph showing olivines (Olv), orthopyroxenes (Opx), clinopyroxenes (Cpx), amphiboles (Amp), spinels (Spl), and a coarse-grained garnet (Grt) with a retrograde reaction rim which is an intergrowth of minerals (kelyphite) (b) Optical micrograph showing a garnet with a kelyphite rim surrounded by a thin rim of coarse orthopyroxenes (COR). Nodular spinels are intermittently located in between the kelyphite and the coarse orthopyroxene rim (c) Optical micrograph showing a matrix clinopyroxene replaced by an amphibole

Fig. 3 Back-scattered electron image of kelyphite with false color. Note the kelyphite largely consists of orthopyroxene (light green) with large patches of clinopyroxene (light blue), small extent of amphibole (green), and vermicular spinel (dark blue)

Fig. 4 Zoning profiles across garnets. Garnet from sample NUM9a without (a) and with (b) a break in scale along the x-axis. Note a decrease in Cr, probably associated with the spinel formation and a subsequent decrease in Al likely related to the kelyphite-forming reaction (c) Garnet in

NRTP4 (d) Garnet in DS0260. Note a decrease in Cr near rims is small in NRTP4 and DS0260 as compared to NUM9a

Fig. 5 Examples of zoning profiles across various minerals. (a) matrix spinel in NRPT4, (b) matrix orthopyroxene, (c) matrix clinopyroxene with no evidence of amphibole replacement, and (d) matrix amphiboles in NRTP4; the right rim of this amphibole is close to the kelyphite relative to its left rim

Fig. 6 (a) Back-scattered electron image of garnet in NUM9a. Note traverse 2 (Tr2) is adjacent to relatively well-developed kelyphite as compared to traverse 1 (Tr1). (b) Zoning profiles across the garnet in NUM9a along traverse 1. (c) Zoning profiles across the garnet in NUM9a along traverse 2. Note a decrease in Cr near rim is distinctive along Traverse 1

Fig. 7 This diagram depicts P-T estimates derived from orogenic peridotite in the Otrøy Island as well as adjacent Flemsøy and Moldefjord (Modified from Spengler et al. 2009). The large gray area indicates the estimates from Otrøy and Flemsøy, and filled circles indicate the estimates from Moldefjord. P-T estimates determined from the samples of this study are also plotted. Note our P-T estimates are in reasonable agreement with the exhumation path of Spengler et al. (2009)

Fig. 8 Amphibole dehydration equilibrium plotted as a function of temperatures and water activities at an the pressure estimated for each sample. The activity of H_2O estimated from amphibole dehydration equilibrium for each sample is plotted as a point along the corresponding curve.

Fig. 9 Activities of four different fluid species in C-O-H system at aC = 1 (a - top) and aC = 0.01 (b - bottom) at a pressure of 24 kbar and temperature of 720 ˚C. Solid lines and dotted lines indicate the results of calculations based on C-O-H equilibria using the approach of Zhang and Duan (2009) and Lamb and Valley (1985) respectively. The vertical lines in each diagram are located at $\Delta\log(fO_2)^{FMQ}$ beyond which aC becomes less than the value of 1 (a) and 0.01 (b). The estimate of aH_2O obtained from pargasite dehydration equilibrium is plotted together at $\Delta\log(fO_2)^{FMQ}$ of sample NRTP4 (see text). The difference in estimates of aH_2O between pargasite dehydration equilibrium and C-O-H equilibria becomes greater at aC decreases (e.g., from 1 to 0.01).

Fig. 10. Compositions of C-O-H fluids calculated at 720˚C and 2.4 GPa are shown by the outermost solid line. Compositions of these fluids at P < 2.4, which implies that the fluid pressure is less than lithostatic, are also shown by solid lines labeled with pressure in GPa (1.5, 1.8, 2.0, and 2.2). Values of oxygen fugacity relative to the FMQ oxygen buffer are shown by the dashed, dotted, and dash-dotted lines. Sample NRTP4 equilibrated at $\Delta\log(fO_2)^{FMQ}$ = -2.2 and aH2O = 0.36 (star) indicating a fluids pressure less than lithostatic (see text).

This is a preprint, the final version is subject to change, of the American Mineralogist (MSA)
Cite as Authors (Year) Title. American Mineralogist, in press.
(DOI will not work until issue is live.) DOI: http://dx.doi.org/10.2138/am-2017-5915

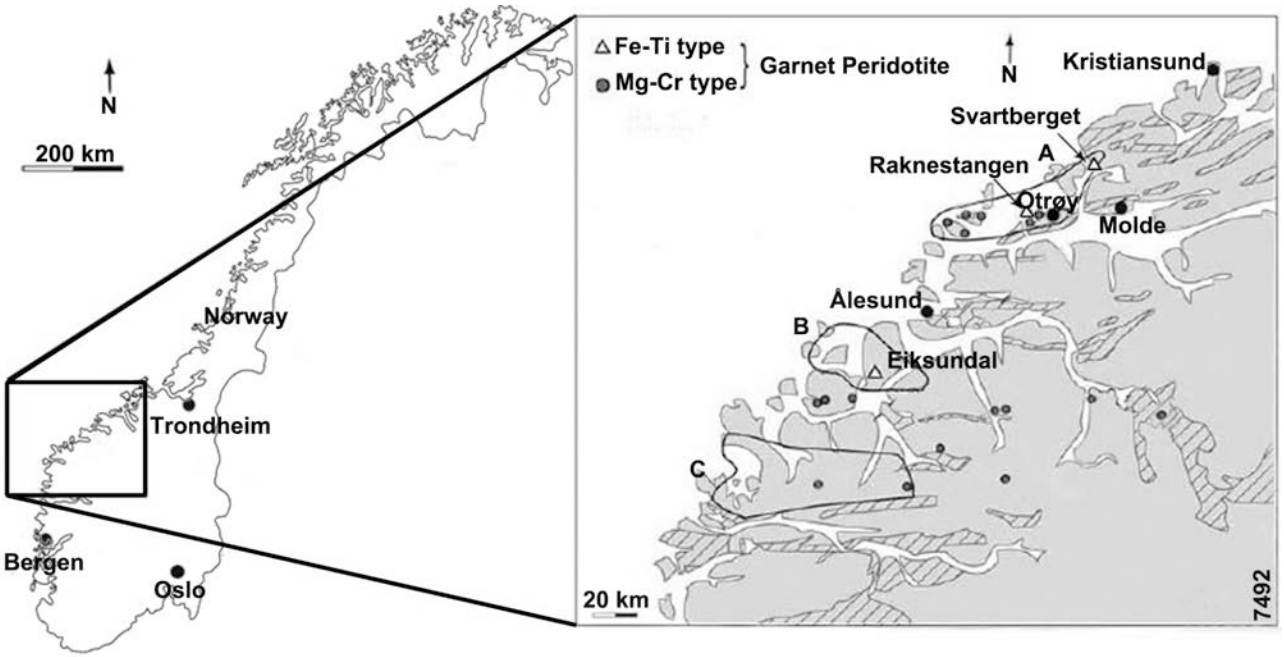

This is a preprint, the final version is subject to change, of the American Mineralogist (MSA)
Cite as Authors (Year) Title. American Mineralogist, in press.
(DOI will not work until issue is live.) DOI: http://dx.doi.org/10.2138/am-2017-5915

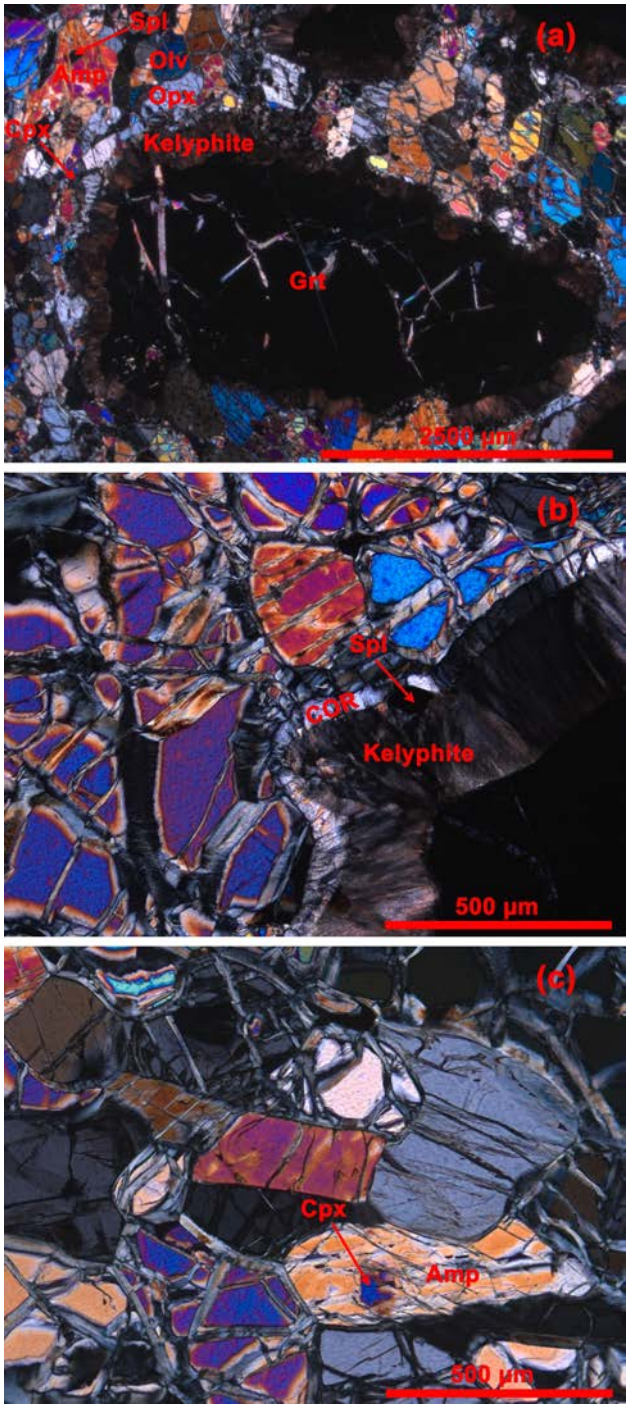

This is a preprint, the final version is subject to change, of the American Mineralogist (MSA)
Cite as Authors (Year) Title. American Mineralogist, in press.
(DOI will not work until issue is live.) DOI: http://dx.doi.org/10.2138/am-2017-5915

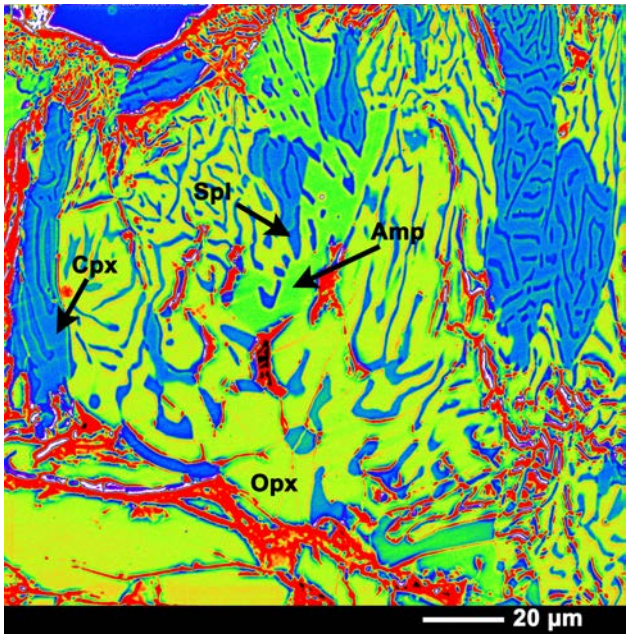

This is a preprint, the final version is subject to change, of the American Mineralogist (MSA)
Cite as Authors (Year) Title. American Mineralogist, in press.
(DOI will not work until issue is live.) DOI: http://dx.doi.org/10.2138/am-2017-5915

Figure 4

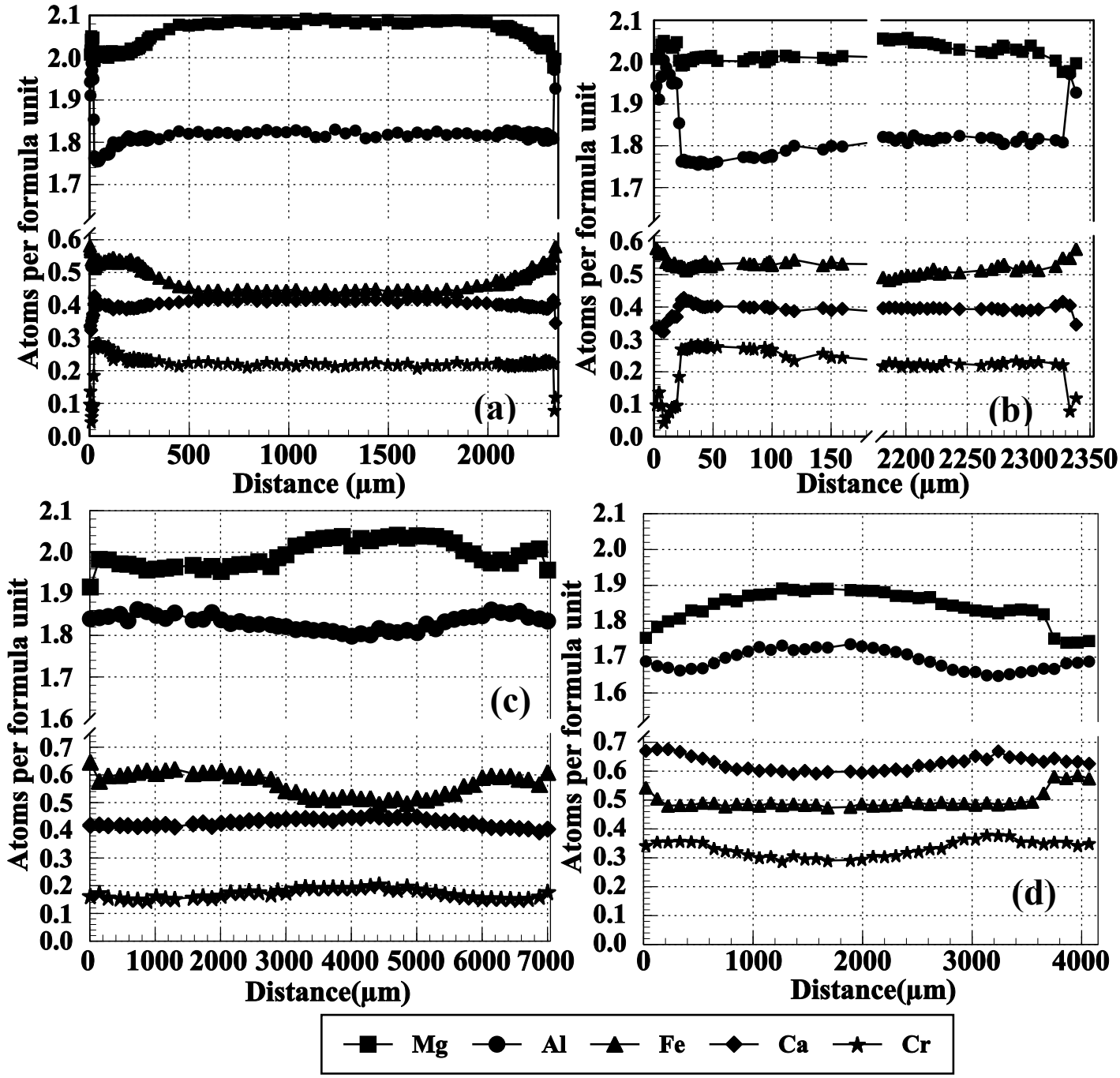

Figure 4. Kang et al.

This is a preprint, the final version is subject to change, of the American Mineralogist (MSA)
Cite as Authors (Year) Title. American Mineralogist, in press.
(DOI will not work until issue is live.) DOI: http://dx.doi.org/10.2138/am-2017-5915

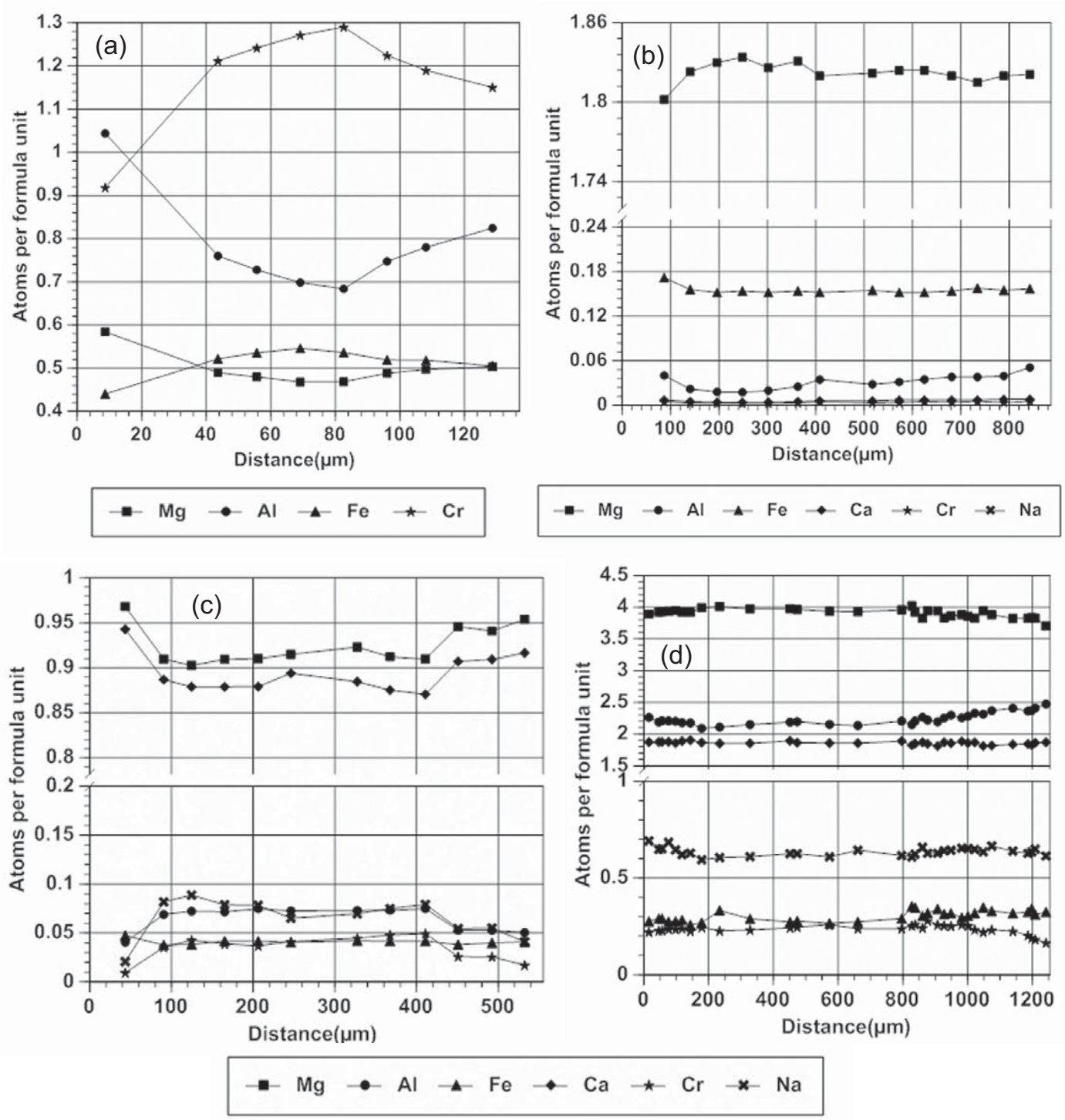

Figure 5 - Kang et al

This is a preprint, the final version is subject to change, of the American Mineralogist (MSA)
Cite as Authors (Year) Title. American Mineralogist, in press.
(DOI will not work until issue is live.) DOI: http://dx.doi.org/10.2138/am-2017-5915

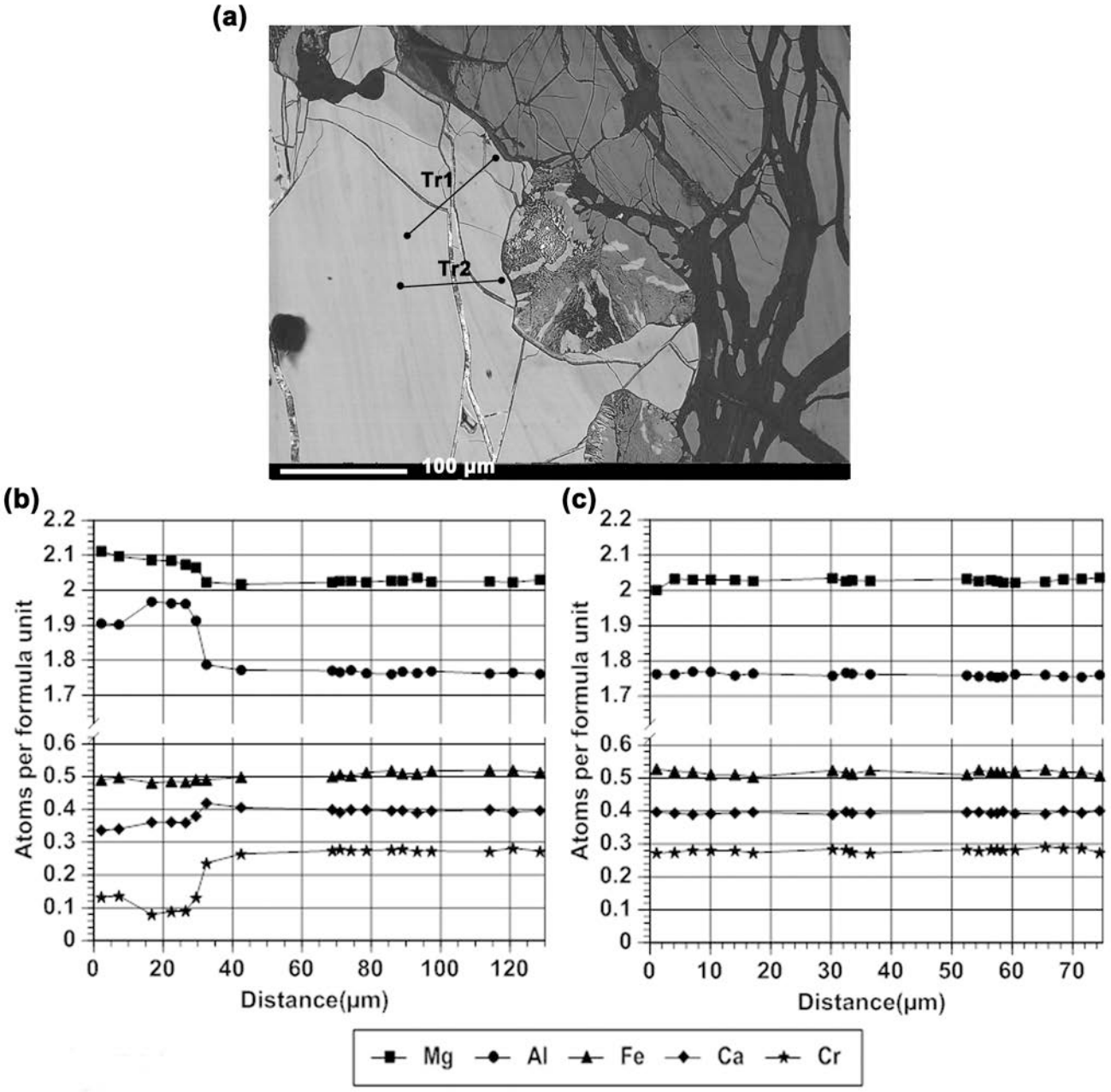

Figure 6 Kang et al.

This is a preprint, the final version is subject to change, of the American Mineralogist (MSA)
Cite as Authors (Year) Title. American Mineralogist, in press.
(DOI will not work until issue is live.) DOI: http://dx.doi.org/10.2138/am-2017-5915

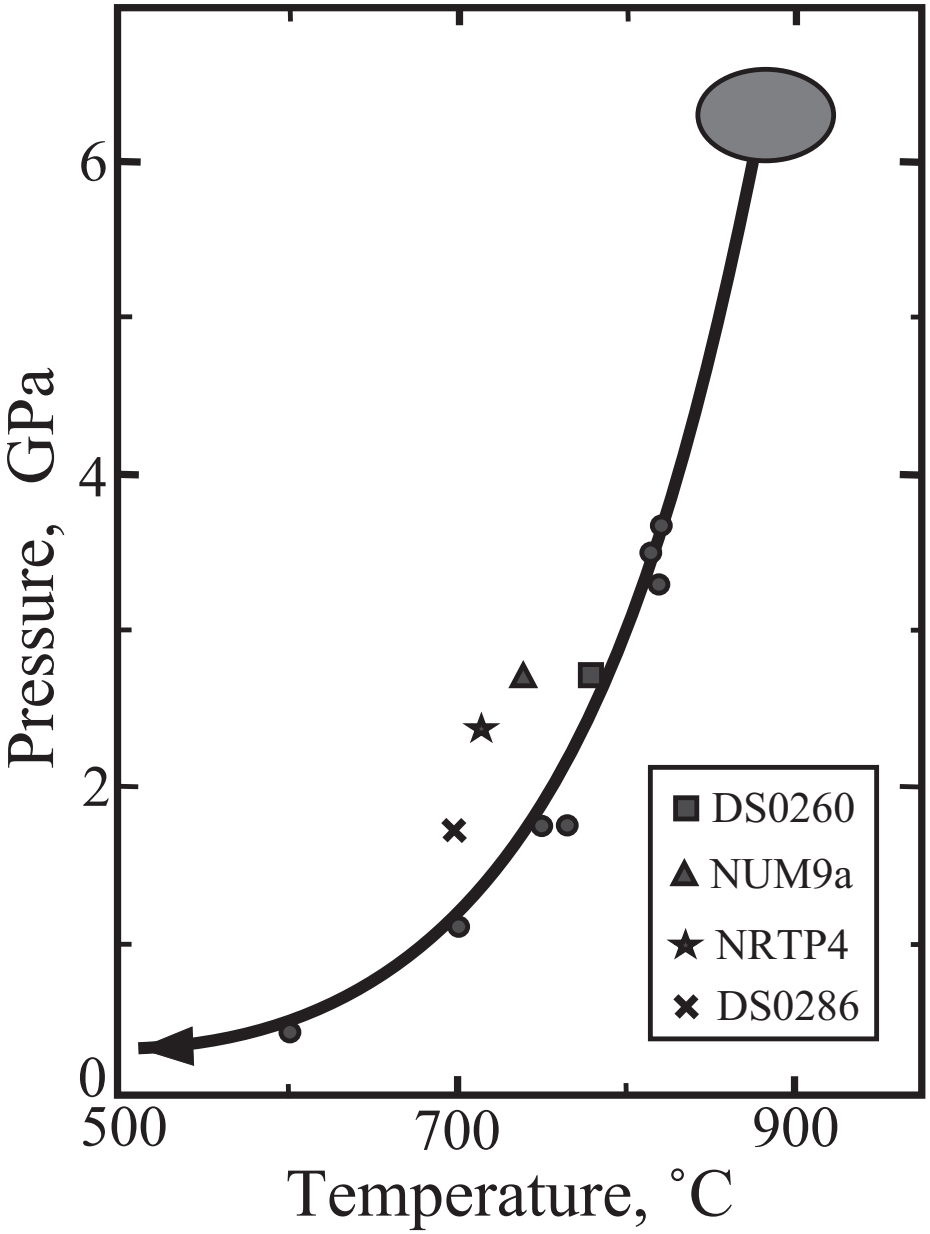

Figure 7 - Kang et al.

This is a preprint, the final version is subject to change, of the American Mineralogist (MSA)
Cite as Authors (Year) Title. American Mineralogist, in press.
(DOI will not work until issue is live.) DOI: http://dx.doi.org/10.2138/am-2017-5915

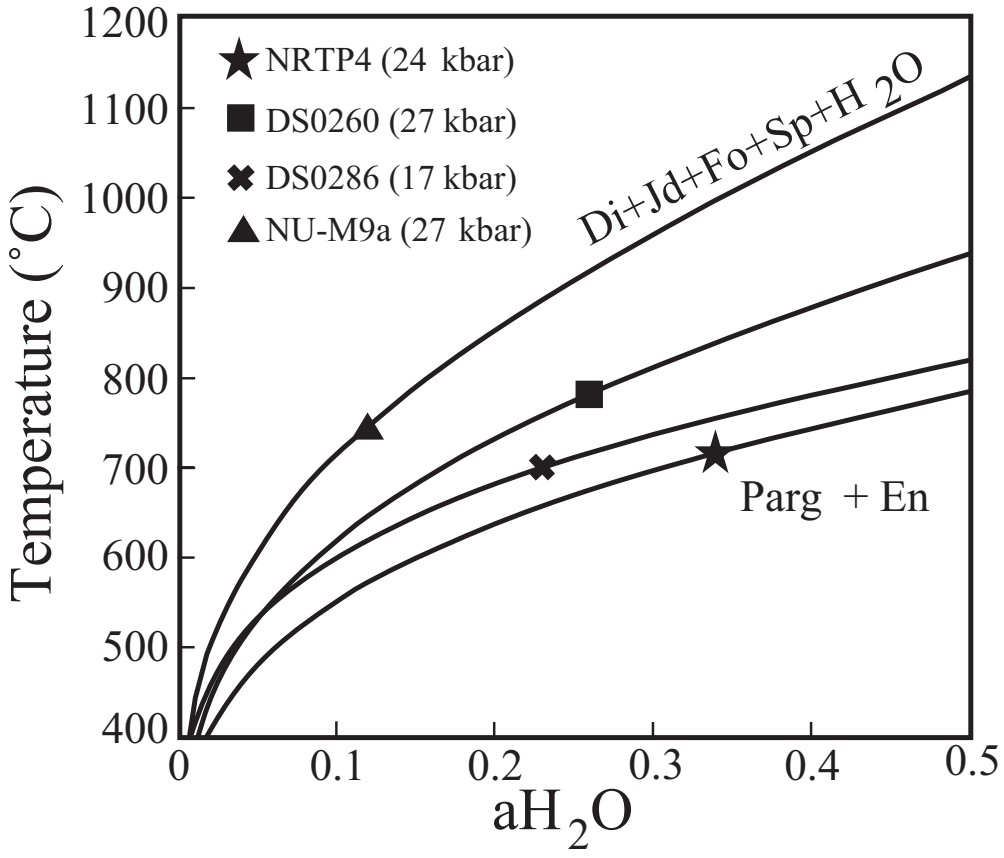

Figure 8 - Kang et al

This is a preprint, the final version is subject to change, of the American Mineralogist (MSA)
Cite as Authors (Year) Title. American Mineralogist, in press.
(DOI will not work until issue is live.) DOI: http://dx.doi.org/10.2138/am-2017-5915

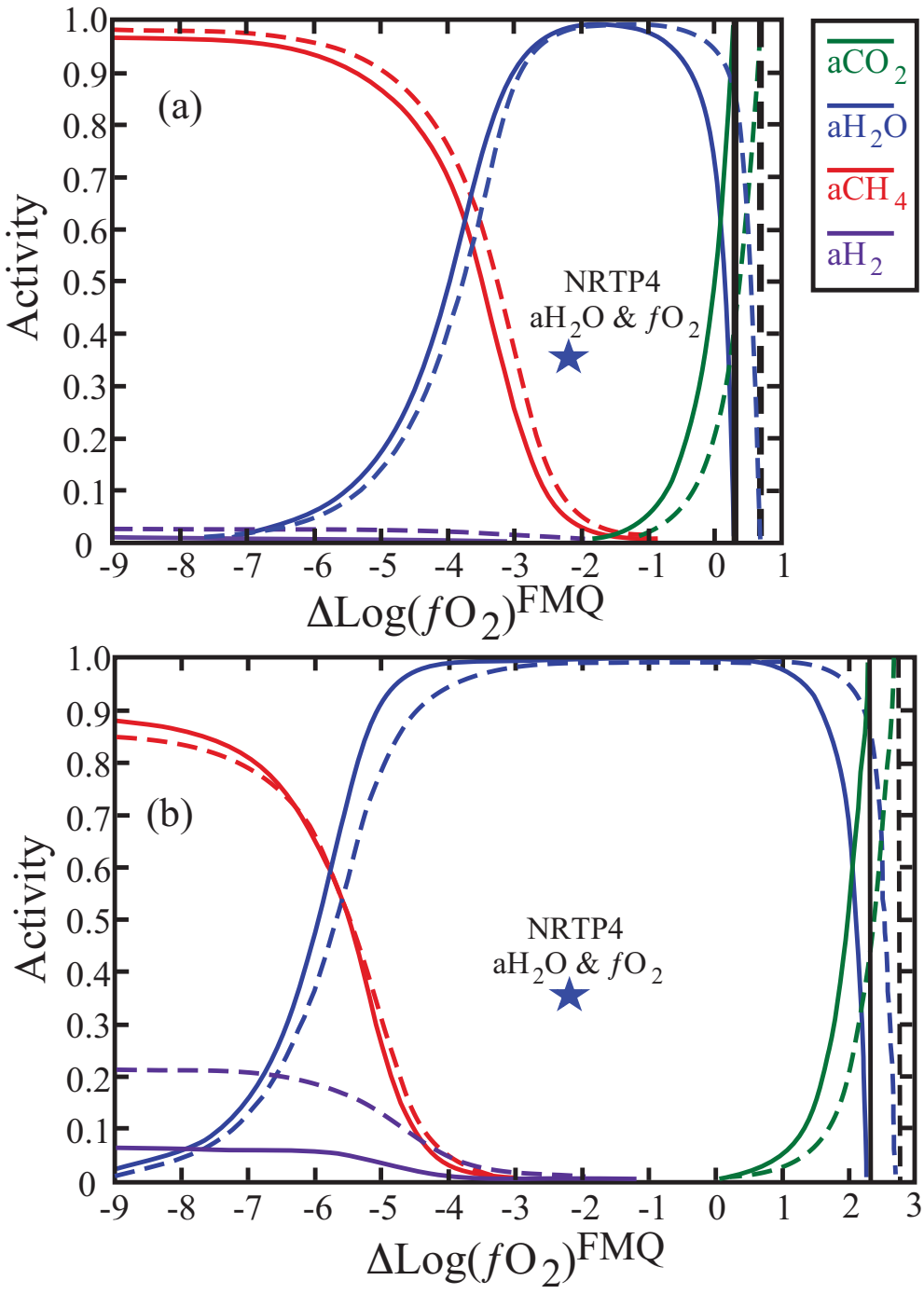

Figure 9 - Kang et al

This is a preprint, the final version is subject to change, of the American Mineralogist (MSA)
Cite as Authors (Year) Title. American Mineralogist, in press.
(DOI will not work until issue is live.) DOI: http://dx.doi.org/10.2138/am-2017-5915